

AD-A104 284

CAMBRIDGE UNIV (ENGLAND) CAVENDISH LAB  
LIQUID IMPACT EROSION MECHANISMS IN TRANSPARENT MATERIALS. (U)  
MAY 81 J E FIELD, S VAN DER ZWAAG, J T HAGAN AFOSR-78-3705

F/6 17/5

AFWAL-TR-81-4026

NL

UNCLASSIFIED

| OF |  
AC:  
410429A

END  
DATE FILMED  
4-10-81  
DTIC

AD A104254

AFWAL-TR-81-4026

(12)

LEVEL II

AD 4267



LIQUID IMPACT EROSION MECHANISMS  
IN TRANSPARENT MATERIALS

Dr. J. E. Field  
S. van der Zwaag  
Dr. J. T. Hagan

Physics and Chemistry of Solids  
Cavendish Laboratory  
Madingley Road  
Cambridge CB3 OHE UK

May 1981

Interim Scientific Report: 30 September 1979 - 30 September 1980

DTIC FILE COPY

Approved for Public Release: Distribution Unlimited

DTIC  
ELECTED  
SEP 16 1981  
S D  
B

MATERIALS LABORATORY  
AIR FORCE WRIGHT AERONAUTICAL LABORATORIES  
AIR FORCE SYSTEMS COMMAND  
WRIGHT-PATTERSON AIR FORCE BASE, OHIO 45433

81 9 16 018

NOTICE

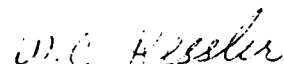
When Government drawings, specifications, or other data are used for any purpose other than in connection with a definitely related Government procurement operation, the United States Government thereby incurs no responsibility nor any obligation whatsoever; and the fact that the government may have formulated, furnished, or in any way supplied the said drawings, specifications, or other data, is not to be regarded by implication or otherwise as in any manner licensing the holder or any other person or corporation, or conveying any rights or permission to manufacture use, or sell any patented invention that may in any way be related thereto.

This report has been reviewed by the Office of Public Affairs (ASD/PA) and is releasable to the National Technical Information Service (NTIS). At NTIS, it will be available to the general public, including foreign nations.

This technical report has been reviewed and is approved for publication.



G. F. SCHMITT  
Project Engineer



W. C. KESSLER, Chief  
Coatings & Thermal Protective  
Materials Branch

FOR THE COMMANDER



F. D. CHERRY, Chief  
Nonmetallic Materials Division

"If your address has changed, if you wish to be removed from our mailing list, or if the addressee is no longer employed by your organization, please notify AFWAL/MLBE, W-PAFB, OH 45433 to help us maintain a current mailing list.

Copies of this report should not be returned unless return is required by security considerations, contractual obligations, or notice on a specific document.

10  
10767  
SECURITY CLASSIFICATION OF THIS PAGE (When Data Entered)

REPORT DOCUMENTATION PAGE		READ INSTRUCTIONS BEFORE COMPLETING FORM
1. REPORT NUMBER AFWAL/TR-81-4026	2. GOVT ACCESSION NO. AD-A104254 (7)	3. RECIPIENT'S CATALOG NUMBER
4. TITLE (and Subtitle) Liquid Impact Erosion Mechanisms in Transparent Materials.	5. TIME PERIOD COVERED Interim Report. 30 Sept 79 - 30 Sept 80	
6. AUTHOR(s) J.E. Field, S. van der Zwaag and J.T. Hagan	7. PERFORMING ORG. REPORT NUMBER AFOSR-78-3705 B	
8. PERFORMING ORGANIZATION NAME AND ADDRESS Physics and Chemistry of Solids Cavendish Laboratory, Madingley Road Cambridge CB3 OHE UK	9. PROGRAM ELEMENT, PROJECT, TASK AREA & WORK UNIT NUMBERS P.E. 62102F, Proj 2422 2422/01 WUN 24220.09	
10. CONTROLLING OFFICE NAME AND ADDRESS AFOSR(PKN) Bolling AFB DC 20332	11. REPORT DATE May 1981	
12. MONITORING AGENCY NAME & ADDRESS (if different from Controlling Office) Materials Laboratory (AFWAL/MLBE) Wright-Patterson AFB OH 45433	13. NUMBER OF PAGES 61	
14. SECURITY CLASS. (of this report)	15. DECLASSIFICATION/DOWNGRADING SCHEDULE	
16. DISTRIBUTION STATEMENT (of this Report)  <b>Approved for public release; distribution unlimited.</b>	17. DISTRIBUTION STATEMENT (of the abstract entered in Block 20, if different from Report)	
18. SUPPLEMENTARY NOTES		
19. KEY WORDS (Continue on reverse side if necessary and identify by block number) liquid impact erosion fracture indentation zinc sulphide PMMA glasses		
20. ABSTRACT (Continue on reverse side if necessary and identify by block number) A study has been made of damage mechanisms caused by liquid drop impact on various infrared transparent solids. Techniques are described for producing liquid jets which simulate the damage produced by impact with spherical drops. Fracture damage to specimens is studied by measuring the post-impact 'residual strength' using a specially developed hydraulic loading test. Damage produced in ZnS by indentation and by impact is discussed in detail. Finally, residual strength curves produced by multiple jet impact are presented; there is a good correlation between experimental data and our theoretical analysis of the process.		

## FOREWORD

This report summarizes research performed at the Cavendish Laboratory, University of Cambridge, Cambridge, England from September 1979 through September 1980 under AFOSR Grant 78-3705. The work was initiated with Laboratory Directors Discretionary Funds, P.E. 61102F and subsequently funded with Project 2422 "Protective Coatings and Materials", Task No. 242201 "Coatings for Aircraft and Spacecraft". The report was submitted in January 1981.

Accession For	
NTIS CR&I	<input checked="" type="checkbox"/>
DTIC TAB	<input type="checkbox"/>
Unannounced	<input type="checkbox"/>
Distribution	
By _____	
Distribution/	
Available Codes	
Dist	Serial
A	

TABLE OF CONTENTS

	PAGE
1. INTRODUCTION	1
2. JET IMPACT ON POLYMETHYL METHACRYLATE	3
2.1 INTRODUCTION	3
2.2 RESULTS	3
3. STUDIES OF CONTACT DAMAGE IN POLYCRYSTALLINE ZINC SULPHIDE	5
3.1 INTRODUCTION	5
3.2 EXPERIMENTAL	6
3.3 RESULTS	7
3.4 DISCUSSION	9
3.5 CONCLUSION	10
4. ZINC SULPHIDE	12
4.1 MATERIAL DESCRIPTION	12
a. Optical analysis	12
b. Crystal structure and crystallographic texture	12
c. Composition	14
4.2 $K_{IC}$ DETERMINATION	15
4.3 LIQUID JET IMPACT DAMAGE ON ZINC SULPHIDE	15
4.4 RESIDUAL STRENGTH MEASUREMENTS	16
a. Unimpacted specimens	16
b. Impact specimens	17
4.5 DESCRIPTION OF THE DAMAGE	17
a. Surface damage	17
(1) $175 \text{ m s}^{-1}$ impact velocity	17
(2) $200 \text{ m s}^{-1}$ impact velocity	18
(3) $300 \text{ m s}^{-1}$ impact velocity	18
(4) $500 \text{ m s}^{-1}$ impact velocity	19
(5) $600 \text{ m s}^{-1}$ impact velocity	19
b. Cross-sectional studies	19
(1) $175 \text{ m s}^{-1}$ impact velocity	19
(2) $300 \text{ m s}^{-1}$ impact velocity	19
(3) $400 \text{ m s}^{-1}$ impact velocity	19
(4) $600 \text{ m s}^{-1}$ impact velocity	19

	PAGE
4.6 DISCUSSION	20
5. MULTIPLE JET IMPACT ON SODA-LIME GLASS	21
5.1 INTRODUCTION	21
5.2 EXPERIMENTAL	21
5.3 RESULTS	22
a. Single liquid jet impact	22
b. Multiple jet impact	23
c. The effect of stress wave reflection and specimen bending	24
5.4 DISCUSSION	24
REFERENCES	28

## LIST OF ILLUSTRATIONS

FIGURE	PAGE
1. Impact on PMMA by jets from a 0.4 mm orifice. (a) $300 \text{ m s}^{-1}$ (b) $400 \text{ m s}^{-1}$ (c) $500 \text{ m s}^{-1}$ (d) $600 \text{ m s}^{-1}$ .	30
2. (a) A schematic diagram of the composite block illustrating the grain orientation and the indentations Q and R respectively along and away from the bulk interface, aa. (b) A schematic diagram of flow lines in the porous zone, pz, and radial, median and lateral cracks, rc, mc and lc, respectively, within the deformed zone, dz. (c) Plot of the mean contact pressure as a function of the ratio of the contact radius to the sphere radius, $a/R$ . The broken line is the elastic curve.	31
3. (a) and (b) show the surface damage around interface and bulk indentations, the interface is marked aa. (c) and (d) reveal grains a,b and c being pushed onto the specimen surface and the intergrannular nature of the dominant radial crack, rc. Both specimens were lightly etched. (e) Subsurface damage of an interface indentation revealing a heavily deformed zone, pz, and traces of median and lateral cracks within the plastic zone.	32
4. (a) and (b) are transmission optical micrographs of the heavily deformed zones, pz, around 150N interface and bulk indentations respectively. There are also traces of median, radial and lateral cracks. (c) and (d) are SEM micrographs at different magnifications of regions in (b) and they illustrate the porous nature of the heavily deformed zone, pz.	33
5. (a) shows the displacement of fiducial line, ff, across the grain boundaries and (b) and (c) show deformation within the grains themselves. The orientation of the grains in (b) is as illustrated in Figure 1(a), while the loading axis in (c) was parallel to the long axis of the grains.	34

## FIGURE

## PAGE

6. (a) and (b) illustrate the spiral flow lines in the porous zone for the larger and smaller grain size material; (c) and (d) are higher magnifications of (a) and show the high void density along the flow lines.	35
7. (a) The "pebble structure" below the surface. (b) Etched cross-section of the specimen, revealing columnar grains ( $2 \times 2 \times 25 \mu\text{m}$ ).	36
8. Diagram of the Debye-Scherrer technique.	37
9. Debye-Scherrer pattern with corresponding lattice parameters for CVD zinc sulphide. The pattern observed is that for the zinc blende or sphalerite structure.	37
10. Zinc blende or sphalerite structure. This structure is closely related to that of diamond.	37
11. Plot of load versus (crack length) $^{3/2}$ for ZnS. The inverse of the slope of the line gives a critical stress concentration factor $K_{IC} = 0.75 \text{ MPa m}^{\frac{1}{2}}$ .	38
12. Diagram of nozzle with curved transition between chamber and orifice. Diameter of orifice was 0.8 mm.	38
13. Semi-elliptical flaw in unidirectional stress field.	38
14. "Residual strength" curve for zinc sulphide for impacts with 0.8 mm diameter jets.	39
15. Equivalent flaw sizes for zinc sulphide as function of impact velocity.	39
16. Equivalent drop sizes for several nozzle diameters.	40
17. 0.8 mm jet impact at $175 \text{ m s}^{-1}$ on ZnS. (a) is an optical transmission micrograph of the impact damage. The flaw leading to failure in the pressure tester is arrowed. (b) is a micrograph for oblique reflective illumination (magnification as in (a)). (c) and (d) are enlargements of the areas marked in (a) and (b) respectively (magnification of (d) as for (c)). (e) and (f) show the specimen after failure in the pressure tester.	41

FIGURE	PAGE
18. 0.8 mm jet impact at $200 \text{ m s}^{-1}$ on ZnS. (a) is an optical transmission micrograph of the impact damage. The flaw leading to failure in the pressure tester is arrowed (b) is a micrograph for oblique reflective illumination (magnification as in (a)). (c) and (d) are enlargements of the areas marked in (a) and (b) respectively (magnification of (d) as for (c)). (e) and (f) show the specimen after failure in the pressure tester.	42
19. 0.4 mm jet impact at $400 \text{ m s}^{-1}$ and $500 \text{ m s}^{-1}$ on zinc-rich zinc sulphide leading to the propagation of residual grinding marks.	43
20. 0.8 mm jet impact at $300 \text{ m s}^{-1}$ on ZnS. (a) is an optical transmission micrograph of the impact damage. The flaw leading to failure in the pressure tester is arrowed. (b) is a micrograph for oblique reflective illumination (magnification as in (a)). (c) and (d) are enlargements of the areas marked in (a) and (b) respectively (magnification of (d) as for (c)). (e) shows the specimen after failure in the pressure tester.	44
21. 0.8 mm jet impact at $500 \text{ m s}^{-1}$ on ZnS. (a) is an optical transmission micrograph of the impact damage. The flaw leading to failure in the pressure tester is arrowed. (b) is a micrograph for oblique reflective illumination (magnification as in (a)). (c) and (d) are enlargements of the areas marked in (a) and (b) respectively (magnification of (d) as for (c)). (e) shows the specimen after failure in the pressure tester.	45
22. 0.8 mm jet impact at $600 \text{ m s}^{-1}$ on ZnS. (a) is an optical transmission micrograph of the impact damage. The flaw leading to failure in the pressure tester is arrowed. (b) is a micrograph for oblique reflective illumination (magnification as in (a)). (c) and (d) are enlargements of the areas marked in (a) and (b) respectively (magnification of (d) as for (c)). (e) shows the specimen after failure in the pressure tester.	46

FIGURE	PAGE
23. cross-sections of 0.8 mm jet impacts (a) 175 m s <sup>-1</sup> , (b) 300 m s <sup>-1</sup> , (c) 400 m s <sup>-1</sup> , (d) 600 m s <sup>-1</sup> .	47
24. Velocity dependence of damage parameters. (a) diameter of undeformed zone, (b) maximum diameter of damaged zone, (c) maximum crack depth.	48
25. 0.8 mm jet impact damage on soda-lime-silica glasses (a) 225 m s <sup>-1</sup> , (b) 300 m s <sup>-1</sup> and (c) 600 m s <sup>-1</sup> .	49
26. Residual strength curve for single 0.8 mm jet impact on soda-lime-silica glass.	50
27. As Figure 26. Data are now plotted separately for "damaged" and "undamaged" specimens.	51
28. Probability of failure due to single 0.8 mm jet impact.	51
29. Results of Figure 26 replotted in terms of equivalent flaw size.	52
30. Residual strength curves for multiple 0.8 mm jet impact on soda-lime-silica glass. (a) double, (b) triple, (c) 5-fold and (d) 10-fold impact per specimen.	53
31. Residual strength curves for single and multiple 0.8 mm jet impact.	54
32. A typical example of the increase of impact damage with number of impacts for a 0.8 mm jet at 250 m s <sup>-1</sup> . (a) after 2 impacts, (b) after 3 impacts, (c) after 5 impacts, (d) after 8 impacts, (e) after 15 impacts, (f) after 23 impacts.	55
33. Residual strength curves for multiple impact. Only results for damaged specimens are plotted.	56
34. Failure probability for multiple impact by 0.8 mm jet.	56
35. Results of Figure 34 replotted in terms of equivalent flaw size.	57
36. Residual strength curves for 3 mm thick soda-lime-silica glass. (a) specimen supported near its edge. (b) specimen acoustically matched to 25 mm thick glass block.	58
37. As Figure 36 but now for double impacts per specimen.	58
38. Schematic diagram of the impact process for a flat ended cylindrical jet.	59

FIGURE	PAGE
39. Predicted crack growth for a single 0.8 mm jet impact on soda-lime-silica glass. Initial flaw size 20 $\mu\text{m}$ .	60
40. Predicted normalised residual strength curve for 0.8 mm jet impact.	60
41. Predicted normalised residual strength curves for 1, 2 and 3 jet impacts per specimen.	61

SECTION 1  
INTRODUCTION

The research on this project is concerned both with developing techniques for the study of liquid impact and with assessing the behaviour of various infrared transparent solids.

As discussed in detail in our previous interim report (1), we use three different techniques for studies of high velocity liquid/solid impact. The first involves projecting specimens of up to 25.4 mm diameter at stationary drops. The second fires a liquid jet at a stationary target. The third uses two-dimensional configurations (discs, wedges of liquid) which are impacted. The first approach is nearest to the practical situation in liquid impact, the second has distinct advantages in its ease of operation, low construction cost and the velocity range which can be covered. The final approach, using the two-dimensional configuration, allows processes occurring inside the impacted liquid to be followed by high-speed photography, and is also nearer situations which can be theoretically analyzed (2).

In order to assess impact damage quantitatively, we measure "residual strengths". This involves impacting a specimen under known conditions and then measuring the strength. A hydraulic apparatus, which stresses 2" (ca. 51 mm) diameter disc specimens, was developed for this (3). The technique has subsequently been modified and improved as was outlined in the last interim report (1,4). The technique can be used for a range of disc sizes; recently we have designed an apparatus for stressing discs of 1" (25.4 mm) diameter. This is proving useful where the amount of specimen material is limited or expensive.

Our earlier work has shown that it is possible to relate drop and jet impact in a useful manner, and to use the concept of an 'equivalent drop size' when impact is with a jet. Our high-speed camera work (1) showed that our apparatus produces jets which are coherent and with smooth, curved front faces. Further, since the high pressures of liquid impact occur in the first instant of impact, jet and drop impact can be made 'equivalent' to a reasonable approximation.

This present report starts by describing jet impact on polymethylmethacrylate (PMMA). Comparisons are made with data published by Adler (5,6) for drop impact on PMMA. Sections 3 and 4 discuss in detail our work on the damage produced in ZnS by indentation and by liquid impact respectively. Finally, Section 5 reports residual strength curves of multiple jet impact. It is

shown that there is a good correlation between the experimental data and our theoretical analysis of the damage process.

## SECTION 2

### JET IMPACT ON POLYMETHYLMETHACRYLATE

#### 2.1 INTRODUCTION

Polymethylmethacrylate (PMMA) has been used extensively in impact work. It was one of the materials used in the early jet impact work in this laboratory (7-10). Fyall and his colleagues at RAE Farnborough also used it to study impact with spherical drops of liquid (11).

It has also played an important role in our work of recent years to place the jet method on a sounder quantitative basis (12-14). Particular advantages are; (1) that it is tough enough to withstand the accelerations and decelerations of impact studies against stationary spherical drops, (2) that it is transparent; and (3) that it can be readily cut and polished, thus allowing cross-sections to be made.

However, having mentioned its many merits, it also has to be noted that PMMA is not particularly representative of other hard polymers as a class of materials. Important differences exist between polymers in their mode of failure. A recent paper (15) from this laboratory, emphasizes some of these differences.

Our recent work has shown that spherical drop impact can be simulated by suitably produced jets (see earlier reports). This has the great experimental advantage that the specimen is stationary and the liquid moves. Early comparison work of jet and drop impact was made by comparing drop and jet damage on PMMA and aluminium and by pressure pulse measurements.

Damage on PMMA was studied by reflection and transmission photography and by taking talysurf (surface profile) traces. Present work is extending this comparison work by broadening the range of velocities and jet configurations used and by cross-sectioning techniques.

#### 2.2 RESULTS

The liquid jet impact damage on PMMA has been studied for impact velocities of 300, 400, 500 and 600 m s<sup>-1</sup>. Examples of the impact damages are shown in Figure 1 for these impact velocities.

The 0.4 mm nozzle with 45° transition between chamber and orifice (Progress Reports 1 and 2) was used throughout this experiment. The jets produced by this nozzle type are 'equivalent' to a 2 mm drop for a wide range of velocities (13,16). The specimens were made from ICI 'Perspex' and had

dimensions of  $60 \times 60 \times 19$  mm<sup>3</sup>. The damage produced is shown for each impact velocity in Figure 1. The resulting damage is in the form of a circular depression surrounding a central undamaged zone. The depression of the central area under impact induces tensile stresses in the material and lead to the formation of a damage ring. This process is analogous to that causing Hertzian fracture.

The area beyond the depressed ring shows many short circumferential cracks. They are nucleated by the expanding Rayleigh wave (10).

The diameter of the central undamaged zone for a  $300$  m s<sup>-1</sup> jet impact is found to be  $0.06$  mm and the outer diameter of the damage site  $1.4$  mm. For  $2$  mm liquid drop impacts on PMMA at  $222$  m s<sup>-1</sup> the inner diameter ranges from  $0.06$  to  $0.75$  mm and outer diameter ranges from  $0.8$  to  $1.5$  mm (5).

The central depression of the undamaged zone was measured with a Talysurf profilometer. For an impact velocity of  $300$  m s<sup>-1</sup>, the depth of the central depression was  $0.15$   $\mu$ m which is in good agreement with the  $0.2$  to  $0.4$   $\mu$ m reported in (5).

At  $400$  and  $400$  m s<sup>-1</sup> impact velocities, the radial flow of the jet erodes the upraised outer edge of the smooth circular depression.

At the highest impact velocity studied in these experiments ( $600$  m s<sup>-1</sup>) deep cracks originate in this ring. For  $2$  mm drop impact, the transition from a largely plastic deformed annulus to a pronounced ring crack was found to occur at the same impact velocity (11).

Talysurf measurements on a  $600$  m s<sup>-1</sup> impact site revealed steps at the intersection of the small circumferential cracks and the surface of the specimen. The vertical side of the step faces the center of the impact. The average height of the step is about  $100$  nm at this impact velocity. This is in good agreement with multiple beam interferometry observations (8,9).

### SECTION 3

#### STUDIES OF CONTACT DAMAGE IN POLYCRYSTALLINE ZINC SULPHIDE

##### 3.1 INTRODUCTION

Recent research on the erosion of brittle solids has been directed towards understanding the role of plastic deformation in producing the crack systems which lead to strength loss and material removal (17-20). It is known that in crystals, dislocation interaction can nucleate the crack systems. A related process has recently been identified in soda-lime glasses, where inhomogeneous shear fault lines can develop, interact, and nucleate the cracks (20,21). The propagation of the cracks is always into the elastic hinterland. In crystalline solids, deformation processes may also be required for the propagation of non-cleavage cracks, such as shear radial cracks in ionic crystals.

In polycrystalline ceramics, the nucleation and propagation of the median, radial, and lateral cracks around plastic indentations are influenced by the grain size and operating temperatures, both of which can significantly affect the erosion behaviour. Changes in grain size and temperature can transfer deformation and cracking modes from within the grain itself to events at the grain boundary, such as sliding and voiding, providing deformation modes for both crack nucleation and propagation.

A recent model for the initiation of microfracture beneath sharp indenters assumes the presence of inherent flaws in the bulk (22). It is, however, possible for the deformation processes themselves to produce the necessary defects for crack growth (21). The assumption of pre-existing cracks is therefore not a necessary one. The present report gives further evidence in support of the important role which the deformation has in creating the stress field and also the defects for the propagation of the crack systems. This means that theories which consider crack nucleation and propagation in a purely elastic matrix have to be used with caution, especially for materials where the propagation of the cracks necessarily requires plastic deformation (23).

The deformation in polycrystalline zinc sulphide, silicon nitride, and various types of silicon carbide by both spherical and Knoop indentations have been examined recently (24-26). It has been observed that the number and extent of lateral cracks around Knoop indentations increased with temperature over the range of  $\sim 20^{\circ}\text{C}$  to  $900^{\circ}\text{C}$  and this was attributed to an increased density of microcracks due to enhanced plasticity at the high

temperatures (26). An observation, hitherto unexplained, which is probably common to most fine-grained brittle polycrystalline solids, is the formation of a porous zone directly beneath the plastic indentation in zinc sulphide and silicon nitride (19,24). Such a porous zone will have a significant effect not only on the mechanical integrity of the component but also on its infrared transparency.

We consider in this report the deformation and cracking processes around Vickers plastic indentations in chemically vapor deposited (CVD)\* zinc sulphide. It will be shown that in quasi-static indentations all the crack systems are contained within the deformed zone; the deformation in this case is by grain boundary sliding and by slip or twinning within the grains themselves. Directly beneath the indentation the intergranular movements are so large as to lead to void formation along maximum shear stress trajectories, and also at their intersection points. The porous zone forms at a mean pressure of 1.5 GPa and an average representative strain of about 2.5%. All the crack systems are nucleated along or at the intersection points of the flow lines or at the boundary of this porous zone. The crack propagation is intergranular.

### 3.2 EXPERIMENTAL

CVD zinc sulphide with columnar grains in the range of  $2 \times 2 \times 25 \mu\text{m}^3$  was supplied by Raytheon. The samples were translucent with a milky yellow color. The average hardness, H, and the critical stress intensity factor,  $K_{IC}$ , (measured from Vickers indentations and from the crack system associated with indentations respectively) were 2.1 GPa and  $0.75 \text{ MPa m}^{1/2}$  respectively. Attempts at sectioning the Vickers impressions by indenting across a pre-existing crack proved unsuccessful because of the roughness of the fracture surfaces. The alternative approach of indenting across the interface (Figure 2a) of two highly polished blocks held rigidly together in a cold mounting plastic was used instead (27). The orientation of the columnar grains in the two clamped specimens was such that the longest axis of the grains was normal to the interface between the specimens. The composite specimens were prised apart after indentation to allow examination of the subsurface damage. Non-interface indentations, such as R in Figure 2a, were also made on bulk material and they were sectioned by sawing and polishing to allow comparison with interface indentations, such as Q. Both

---

\*For a detailed description of the ZnS used, see Section 4 of this report.

optical and scanning electron microscopy (SEM) were used to examine the surface and subsurface damage. Spherical indentations at different loads with 800  $\mu\text{m}$  diameter tungsten carbide spheres were also made on zinc sulphide and the residual contact diameter measured. From the measurements it was possible to determine the stress-strain curve (and hence the yield stress) and the corresponding strain for the onset of porosity in the heavily deformed zone directly beneath the indenter. The strain is defined as a constant times the ratio of the contact radius,  $a$ , to the ball radius,  $R$ .

### 3.3 RESULTS

The surface and subsurface deformation around 300N interface and bulk indentations are compared in Figure 3. The surface around the indentation is characterized by a dimpled region (clearer and arrowed in Figure 3b) which marks the size of the plastic zone. The radial cracks,  $rc$ , emanate from the corner of the plastic impression and extend as far as the plastic zone. One pair of radial cracks in Figure 3a coincides with the interface,  $aa$ , but apart from this the surface damage in the two cases is essentially the same. The dominant deformation mode is grain boundary sliding as can be seen in region Q of Figure 3c, which is an SEM micrograph of a region close to the indentation  $sss$ . Also apparent is the intergranular nature of propagation of the main radial crack,  $rc$ . Figure 3d again reveals the intergranular radial crack propagation. The subsurface damage of an interface indentation (Figure 3e) shows traces of lateral cracks and radial and median cracks, ( $rc$  and  $mc$  respectively) which form at different stages of the loading cycle. The median cracks form first, while the lateral cracks,  $lc$ , only develop during the unloading cycle.

All the crack systems emanate from a heavily deformed zone,  $pz$ , directly beneath the plastic impression and within the plastic zone. The deformed material surrounding the indentation consists of two zones, namely a spherical zone,  $pz$ , whose radius is equal to the diagonal length of the plastic impression and a second larger zone,  $dz$ , which extends to the ends of the radial cracks. This second region is the size of the overall plastic zone and the deformation in this case is by grain boundary sliding and reorientation in the indentation stress field. Towards the center of the deformed zone, the intergranular displacements become large enough to lead to void formation and the development of a porous zone,  $pz$ . This is clearly evident in Figures 4a and b which show transmission optical micrographs of heavily deformed zones around 150N bulk and interface indentations respectively.

The broken arrows mark the size of the porous zone near the specimen surface (the continuous white line). There are traces of median, radial, and lateral cracks around the porous zone. The voids in the porous zone scatter the light and therefore appear as black spots. Note that the pore density increases towards the center of the zone,  $p_z$ . The voids in the porous zone are shown in greater detail in the SEM micrograph in Figure 4d which is a higher magnification of a region in Figure 4c. The voids, V, at the boundaries, are clearly formed by grain boundary sliding. Away from this porous zone the sliding occurs without any void formation. This grain boundary sliding is more evident in Figure 5a which illustrates the displacement of fiducial lines, ff, across the grain boundary. The void formation may require some deformation within the grains themselves. The deformation within the grains is more apparent in Figures 5b and c which show regions in the subsurface indentations with the loading axis normal to (such as Figure 2a) and along the axis of the longest axis in the grains a and b. There are also voids along the columns of grains.

Another observation in the porous zone is the development of what appear to be spiral flow lines. Figure 6a shows the subsurface damage for a 150N Vickers indentation in which the preferential void formation along the flow lines makes them just discernable. The flow lines are evident for a 300N indentation on a smaller grain  $0.5 \times 0.5 \times 5 \mu\text{m}^3$  zinc sulphide specimen as in Figure 6b. Median and radial cracks can also be seen in these figures. The width of the distorted zone along the flow lines is influenced by the grain dimensions; the smaller the grain size, the larger and more localized the distortion will be. The flow lines are therefore clearer in the smaller grain material. Higher magnifications of the flow lines in Figure 6a are arrowed in Figure 6c and they show the high void density along the flow lines and also the nature of the pores between the grains as in Figure 6d. All the features in the subsurface deformed zone are illustrated schematically in Figure 2b.

The stress-strain curve obtained from spherical indentations on zinc sulphide is illustrated in Figure 2c. The broken line through the origin is the elastic curve from Hertz's analysis (28). It was difficult to obtain reliable estimates of the contact radius at low pressures (up to 1.2 GPa) and the experimental curve has been extrapolated to the elastic curve. The yield stress defined as the point of departure from the elastic behavior is 0.68 GPa. By studying the cross-sections of indentations formed in different loads, the stress and strain at which the porous zone starts to

develop have been established as 1.5 GPa and 2.5% respectively.

### 3.4 DISCUSSION

Contact damage in CVD zinc sulphide shows all the characteristic features of indentations in isotropic elastic/plastic solids; namely, the deformed zone and median, radial, and lateral cracks. The deformation is accommodated by slip in the grains and grain boundary sliding which leads to nucleation of voids/crack nuclei and propagation of the various crack systems. Since the deformation process is required for the propagation of the cracks, all the cracks are contained within the plastic zone and do not extend into the elastic hinterland as occurs, for example, in soda-lime glass.

The most interesting observation within the deformed zone is the existence of a porous region,  $p_z$ , directly beneath the indenter (see Figure 4). It has been established very clearly with Figure 4d that the zone,  $p_z$ , is made of voids, formed by the very large displacement of the grains in the region. All the crack systems emanate from around this porous boundary and are nucleated from such voids.

A closer examination of the porous zone has shown the development of shear flow lines which are similar to the inhomogeneous flow lines in soda-lime glass (20) and around punch indentations in metals and paraffin (29). The flow lines follow the maximum shear stress trajectories that occur around a pressurized cylindrical tube in a plastic body. Thus, under quasi-static pyramidal indentations and for the particular orientation of the grains (Figure 2a), zinc sulphide behaves in an ideally isotropic elastic/plastic manner. The flow lines exist in the whole plastic zone but the preferential pore formation along the flow lines makes them clearer in the porous zone. This high void density along the flow line is clearly visible in Figure 6c and d. It therefore appears that the flow lines form first and as the displacements along these build up and the flow lines start intersecting with each other, voids develop along the shear trajectories and at their intersection points. These in turn provide nuclei for the median, radial, and lateral cracks as suggested for soda-lime glass (20).

By the principle of geometric similarity the mean indentation pressure,  $P$ , is given by

$$P = f(a/R) \quad (1)$$

where  $a/R$  is the ratio of the contact radius to the indenter radius. For

the purely elastic case, this takes the form of

$$P = \frac{8}{3\pi} G_1 \frac{a}{R} [(1 - v_1) + (1 - v_2) G_1/G_2]^{-1} \quad (2)$$

after simplifying Hertz's equation for the relationship between the contact radius,  $a$ , and the mean pressure,  $P$ .  $G_1$ ,  $v_2$  and  $G_2$ ,  $v_2$  in equation 2 are the shear modulus and Poisson ratio for the specimen and indenter materials respectively.

The dotted line in Figure 2c is the theoretical curve plotted from equation 2. The point of departure of the experimental curve from the elastic curve occurs at ca. 0.86 GPa which is in good agreement with the yield stress of 0.70 GPa obtained from the Vickers hardness of 2.1 GPa, assuming  $H = 3Y$ .

It has been shown empirically (30) that once the fully plastic stage is reached ( $P/Y \approx 3$ ), the average representative strain  $\epsilon$ , in percent, is given by

$$\epsilon = 0.2 \left[ \frac{a}{R} \right] \quad (3)$$

In Figure 2c the above relationship is only applicable to values of  $a/R > 0.6$  for which the pressure tends to the Vickers hardness. The strain in the region between the elastic limit and the fully plastic case is not adequately defined by the above relationship. In this report, however, equation 3 is used to represent the average representative strain.

Also, from studies of cross-sectional views of these spherical indentations at difference loads, we have established that the porous zone forms at a strain of ca. 2.5% and is fully developed at a mean pressure of 1.7 GPa which is more than twice the yield stress. This strain value is consistent with the observation that a porous zone is always associated with a Vickers indentation for which there is a constant representative strain of 8% irrespective of the load (30).

### 3.5 CONCLUSION

The observations indicate that during static indentations in CVD zinc sulphide the deformation is accommodated by grain boundary sliding and by deformation within the grains themselves. The total deformation extends up to the tips of the radial cracks and it is about 2-3 times the size of the

porous zone from around which all the cracks emanate. For the particular grain orientation studied, the material behaves in an ideal elastic/plastic manner, with the development of spiral flow lines in the region directly beneath the indenter. As the displacement along the flow lines increases, the grains are sheared past each other, leading to decohesion and void formation. This explains the origin of the porous zone observed under pyramidal indentations in zinc sulphide and silicon nitride (24). The grain boundary sliding probably also explains the enhanced lateral cracking in silicon carbide at higher temperatures (26), since the sliding process will become easier at the higher temperatures and lead to more voids and cracks.

From the erosion and strength degradation point of view, polycrystalline materials provide energy-dissipative mechanisms by grain boundary sliding and cracking. An ideal material for this type of contact loading would be one in which appreciable energy dissipation occurs within the grains as well as at their boundaries. It appears that there should exist a critical grain size for which this is possible.

A problem that has to be considered seriously is the effect of the porous zone on the infrared transparency even in the absence of any strength degrading cracks. This is important especially in situations where the transparency is a critical factor in design.

These studies, together with previous work on soda-lime glass and ionic crystals have revealed two different types of material response to static indentation with sharp indenters. In the first, the deformation process is required for the crack nucleation only, and the subsequent crack propagation is into the elastic hinterland. In the second, the plastic deformation is necessary for both the nucleation and propagation of the various cracks so that the crack systems are contained within and limited by the plastic zone. The zinc sulphide studied in this work fell into the latter category.

SECTION 4  
ZINC SULPHIDE

4.1 MATERIAL DESCRIPTION

a. Optical analysis

The zinc sulphide specimens available for liquid jet impact experiments were produced by the Raytheon Corporation by a CVD process. No information about the deposition process, in particular the deposition temperature and deposition rate, is available. The specimens are translucent with a milky-yellow color. Local fluctuations in the transparency are easily observable with the naked eye; Figure 7a gives a low magnification optical photograph. The fluctuations are caused by the "pebble" structure formed on the surface during deposition. Large differences in size and intensity of the "pebble" structure have been observed between individual specimens. Small black inclusions (average size ca.  $2 \times 2 \times 2 \mu\text{m}^3$ ) have also been observed. The average density of the inclusions is about 10 per  $\text{cm}^3$ . The presence of a "haystack" structure around the inclusions was observed which indicates that heterogeneous nucleation on a microscopic scale occurs.

Etching of the specimens in a Bromine-Methanol (1 to 10 by volume) solution revealed a columnar grain structure (Figure 7b). The axis of the columnar grains is normal to the specimen surface, i.e. normal to the plane of deposition. The average grain dimensions are  $2 \times 2 \times 25 \mu\text{m}^3$  and the variation in size is small.

b. Crystal structure and crystallographic texture

The Debye-Scherrer technique, which is illustrated schematically in Figure 8 was used to determine the crystal structure of CVD zinc sulphide. In this technique, a collimated monochromatic X-ray beam is reflected by a fine-grained polycrystalline specimen positioned in the center of the Debye-Scherrer camera. For the particular film position shown in the figure, the Bragg reflection angle is given by

$$\theta = \frac{L}{2R} \quad (4)$$

where  $\theta$  = Bragg reflection angle

L = distance on the film between reflection ring and

R = radius of the Debye-Scherrer camera beam.

### Using the Bragg condition for reflection

$$\lambda = 2d \sin \theta \quad (5)$$

where  $\lambda$  = wavelength of incident radiation

$d$  = interplanar spacing in crystal lattice and

$\theta$  = Bragg angle,

the interplanar spacing  $d$  can be determined. Since the series of interplanar spacings together with the relative intensities of the rings are a characteristic material property, the technique is suitable for the determination of the composition and crystal structure of a specimen.

The Debye-Scherrer pattern obtained for CVD zinc sulphide, shown in Figure 9 with the corresponding lattice indices, is that for the cubic modification of zinc sulphide, called zinc blend or sphalerite. This structure (Figure 10) has the same Bravais lattice as diamond. Other structures of zinc sulphide are the hexagonal structure (wurtzite) which is stable above 1000°C and a rock-salt type structure with octahedral coordination of cations and anions. This latter structure can only be formed at very high pressures (31). Several other polytypes of zinc sulphide with mixed packing of the anions have been found as minerals (32) or have been synthesized (33). Crystalline disulphides (34) and amorphous polysulphides (35) are also known.

The Debye-Scherrer pattern in Figure 9 also shows the presence of a preferential crystal orientation or texture (clearest in the (200) reflection ring). Since the patterns are identical for the front and back surface, the texture is assumed to be throughout the specimen thickness.

Detailed X-ray reflection measurements with a texture goniometer have confirmed that the texture is well-defined. The texture is mainly of a (100) nature i.e., for most crystals the <100> direction is normal to the surface of the specimen and hence parallel to the axis of the columnar grains. A very weak (221) texture perpendicular to the surface has also been determined. No preferential crystal orientation in the plane of the surface could be determined.

The sharpness of the Debye-Scherrer rings further indicates the absence of both large internal strains and of polytypes of zinc sulphides.

c. Composition

The composition of the CVD zinc sulphide specimens has been determined by X-ray microanalysis (Applied Research Laboratory electronprobe microanalyzer with X-ray spectrometers). The results of the analysis are:

zinc:             $68.0 \pm 0.2\%$             (weight percent)  
or                 $50.1 \pm 0.2\%$             (atom percent)

sulphur:           $33.1 \pm 0.1\%$             (weight percent)  
or                 $49.8 \pm 0.1\%$             (atom percent)

Reference materials used in the X-ray microanalysis are pure zinc and iron disulphide for the zinc and sulphur determination respectively.

The oxygen and iron contents in the specimen were below the detection levels of the microanalyser i.e., less than 0.08% relative to the silicon dioxide and less than 0.03% relative to pure iron respectively. The carbon content has not been determined.

#### 4.2 $K_{IC}$ DETERMINATION

The critical stress intensity factor,  $K_{IC}$ , has been determined with the Vickers indentation technique. It has been shown that the relation between  $K_{IC}$  and the induced crack length (36) is

$$K_{IC} = \chi P/c^{3/2} \quad (6)$$

where

$$\chi = (\pi^{3/2} \tan \psi')^{-1} \quad (7)$$

and

$$\psi' = \psi + \tan^{-1} \mu \quad (8)$$

the terms in these equations are defined as:

P is applied load  
c is crack length

$\psi$  is indenter semi-angle ( $68^\circ$ )

$\mu$  is coefficient of friction between indenter and specimen.

A typical plot of load versus  $c^{3/2}/\chi$  is shown in Figure 11. The  $K_{IC}$  value is given by the inverse of the slope of the least mean squares regression fit. The value of the coefficient of friction between indenter and specimen is assumed to be zero. The average  $K_{IC}$  value determined is  $K_{IC} = 0.75 \text{ MPa m}^{\frac{1}{2}}$  (fracture surface energy =  $3.4 \text{ J m}^{-2}$ ). This result agrees well with those reported in the literature (37-40).

#### 4.3 LIQUID JET IMPACT DAMAGE ON ZINC SULPHIDE

For the liquid jet impacts on zinc sulphide, the 0.8 mm nozzle with curved transition between chamber and orifice has been used (Figure 12).

The specimens were supplied in the form of discs (50 mm diameter; 3.0 mm thick). The specimens were polished to optical quality. No surface scratches were discernable. Before impact the specimens were mounted in a newly developed specimen holder which ensures a central impact on the specimen. Also the distance between the nozzle exit and specimen surface is fixed at the ideal stand-off distance of 10 mm. To reduce the effect of reflected stress waves from the back surface on the impact damage, specimens were acoustically matched to a 1 cm thick zinc sulphide disc.

#### 4.4 RESIDUAL STRENGTH MEASUREMENTS

The residual strength of zinc sulphide specimens after liquid jet impact was measured with the hydraulic pressure tester (3,4). The improved stress analysis (Progress Report 1, (4)) was used to calculate the fracture stress.

From the fracture stresses, the equivalent flaw sizes have been calculated assuming a semi-elliptical crack in a unidirectional tensile stress field (Figure 13). For this stress field and crack geometry, the relation between crack size,  $c$ , and fracture stress,  $\sigma_f$ , is given by (41)

$$K_{IC} = 1.16 \sigma_f \sqrt{c} \quad (9)$$

where  $K_{IC}$  is the critical stress intensity factor. For this grade of zinc sulphide, the  $K_{IC}$  value is  $K_{IC} = 0.75 \text{ MPa m}^{\frac{1}{2}}$  as determined by the indentation technique.

a. Unimpacted specimens

The fracture stresses and equivalent flaw sizes for 8 unimpacted zinc sulphide specimens are given in Table 1. The average stress is 67.5 MPa with a standard deviation of the mean of 5.0 MPa. The scatter in the data points is considerable. This average fracture stress value is lower than that reported in (40),  $\sigma_f = 100$  MPa. The average equivalent flaw size is 184  $\mu\text{m}$ .

The large equivalent flaw size (about 100 times the grain diameter) suggests that the damage produced during the grinding operation is insufficiently removed during the subsequent polishing operation. No relation between crack nucleating flaws and pebble structure has been found.

TABLE 1 FRACTURE STRESSES FOR UNIMPACTED ZnS

Fracture stress/MPa	Equivalent flaw size, $2c/\mu\text{m}$
56.8	158
95.2	92
60.5	228
59.6	234
61.3	222
81.8	124
54.7	278
69.8	170

b. Impact specimens

The fracture stress of zinc sulphide as a function of impact velocity for an 0.8 mm jet is plotted in Figure 14. The same data are plotted as equivalent flaw size in Figure 15. No reduction in strength was observed at and below an impact velocity of  $125 \text{ m s}^{-1}$  for the 8 specimens tested in this region. In this series only two specimens failed due to a defect near the center of the specimen. However their strength was higher than the average strength for unimpacted specimens. Therefore all the specimens are regarded as undamaged by the impact. The new average fracture stress for undamaged specimens is now

$$\sigma_f = 76.1 \pm 4.0 \text{ MPa}$$

The scatter in fracture stress is rather large with a minimum value of 54 MPa

and a maximum value of 113 MPa. For impact velocities of  $150 \text{ m s}^{-1}$  to  $600 \text{ m s}^{-1}$  all specimens failed centrally indicating that the impact did damage the specimen. Due to the limited number of specimens available, the velocity dependence of the fracture stress could not be determined accurately in this velocity region.

The equivalent drop size curve for the new nozzle type has not been determined yet. It is therefore at present not possible to convert the measured residual strength curve into a residual strength curve for 2 mm drop impact. The equivalent drop size determined by Richerby (Figure 16) based on earlier nozzles (16) shows that the equivalent drop size increases rapidly for impact velocities below  $200 \text{ m s}^{-1}$ . At that time it was not possible to fire jets below  $300 \text{ m s}^{-1}$  so that the low velocity part of the curve was determined by extrapolation. The assumption that the 0.8 mm jet impact is equivalent to a 4 mm drop impact over the whole velocity range investigated gives a threshold velocity for 2 mm drop impacts of about  $175 \text{ m s}^{-1}$ . This is calculated using the relation that  $(\text{velocity})^2 \times \text{drop diameter}$  is approximately constant. Such a value would be in good agreement with a threshold velocity for 3 mm diameter drop impact of  $175 \text{ m s}^{-1}$  (42).

#### 4.5 DESCRIPTION OF THE DAMAGE

##### a. Surface damage

The surface damage for the new nozzle type was described for impact velocities between 150 and 600 m s<sup>-1</sup>.

###### (1) $175 \text{ m s}^{-1}$ impact velocity

The impact damage at  $175 \text{ m s}^{-1}$  is shown in Figure 17 a and b. A ring of short circumferential cracks around an unbroken central zone is observed. The ring cracks are shown in more detail in Figures 17 c and d. The residual fracture stress of this specimen was 47.0 MPa with an equivalent flaw size of 350  $\mu\text{m}$ .

Examination of the specimen after fracturing in the pressure tester (Figures 17 e and f) allowed the flaw which led to failure to be found (arrowed in Figure 17 a). This flaw is at the outer edge of the damaged zone. The measured crack length for this flaw, about 300  $\mu\text{m}$ , agrees well with the calculated equivalent flaw size.

###### (2) $200 \text{ m s}^{-1}$ impact velocity

The impact damage for a  $200 \text{ m s}^{-1}$  jet is shown in Figure 18. The

dimensions of the damaged zone have increased but more important is the propagation of two severe surface flaws. The damage around one of these cracks is shown in more detail in Figure 18 c and d. Upon testing, a very low fracture stress of 31.2 MPa was determined for this specimen due to the presence of the large cracks. As shown in Figures 18 e and f, these large flaws led to failure.

The long cracks observed on this specimen are very similar to those observed on ZnS specimens obtained from other sources as shown in Figure 19. For these particular specimens, the unidirectionality of surface flaws suggested that the flaws were due to the grinding process. During the subsequent polishing process, the grinding damage was insufficiently removed. This mechanism is also proposed for the specimen tested in this experiment. The mechanism would also give an explanation for the observed large scatter in fracture stresses for undamaged specimens.

#### (3) 300 m s<sup>-1</sup> impact velocity

The impact damage for a 300 m s<sup>-1</sup> impact is shown in Figure 20. The impacted area was free of major surface defects resulting in a symmetric damage pattern. Both the crack density in the ring around the central zone and the extent of the damaged area have increased. Comparison of the transmission micrographs (20 a and c) and the reflection micrographs (b and d) show clearly that material removal due to radial jetting of the jet only occurs in a relatively small region of the damaged area. Again a crack at the outer edge of the damaged zone led to failure of the specimen during fracture in the pressure tester as can be seen from Figure 20 e. The calculated equivalent flaw size of 520 mm agrees reasonably well with the observed flaw size.

#### (4) 500 m s<sup>-1</sup> impact velocity

Figure 21 shows the damage after a 500 m s<sup>-1</sup> jet impact. Both total damaged area and the average crack length and density have increased considerably in comparison with a 300 m s<sup>-1</sup> jet impact. The increase in damage is particularly clear in Figures 21 c and d. This specimen contained a serious surface flaw in the impacted area. Figure 21b shows that gross material removal did occur at this flaw. The curvature of this flaw suggests that the damage is caused during the handling of the specimen.

(5)  $600 \text{ m s}^{-1}$  impact velocity

Finally, the impact damage at  $600 \text{ m s}^{-1}$  is shown in Figure 22. An even further increase in damage especially in the heavily cracked ring around the undeformed center is observed. Again a crack at the outer edge of the damaged zone led to specimen failure (Figure 22e). In the center of the "undamaged" zone a damage mark due to Munroe jetting can be discerned. However this does not influence the damage pattern or the residual strength of the specimen.

b. Cross-sectional studies

Cross-sectional studies of impact sites for  $0.8 \text{ mm}$  jets at different impact velocities have been made to determine the crack profile.

(1)  $175 \text{ m s}^{-1}$  impact velocity

A top and cross-sectional view through the center of a  $175 \text{ m s}^{-1}$  jet impact site is shown in Figure 23a. The innermost fractures, closest to the undeformed zone, are very short and approximately straight. The angle between the cracks and the surface is about  $80^\circ$ . Progressing radially outward, the depth of the cracks increases gradually. However, the angle between crack and surface decreases.

The interaction of the Rayleigh surface wave with a major surface defect on the left of an impact site not only caused crack extension on the surface but also considerable crack growth normal to the surface.

(2)  $300 \text{ m s}^{-1}$  impact velocity

The features displayed at this impact site (Figure 23b) are essentially the same as for the  $175 \text{ m s}^{-1}$  impact although the cracks have increased both in number and in depth. The innermost cracks tend to curve towards the normal on the surface. Cracks in the middle of the damaged zone are curved towards the free surface. Double curvature in these cracks has also been observed. The outermost cracks are normal to the surface.

(3)  $400 \text{ m s}^{-1}$  impact velocity

The damage due to a  $400 \text{ m s}^{-1}$  jet impact is shown in top and cross-sectional views in Figure 23c. The depth of the cracks in the ring zone has further increased. The curvature of the cracks is more pronounced than for the  $300 \text{ m s}^{-1}$  jet impact but essentially similar.

(4)  $600 \text{ m s}^{-1}$  impact velocity

The impact damage for a  $600 \text{ m s}^{-1}$  jet impact on an unsupported  $3 \text{ mm}$  thick sheet of ZnS is shown in Figure 23d. The stress wave reflection on the free

bottom surface caused cracking on and just below the surface (spalling). The reflected bulk stress wave also interacted with the deepest cracks nucleated at the impacted surface. Hence, cracks parallel to the free surface are formed below the center of the impact. These cracks lead to a drastic loss in transmission of the specimen. The cracks nucleated at the surface are similar to those discussed previously. This figure shows that the damage is not only determined by the jet size and velocity but also by the specimen dimensions in particular the specimen thickness.

#### 4.6 DISCUSSION

The cross-sectional fracture pattern for liquid jet impacts with impact velocities between 175 and 600 m s<sup>-1</sup> agrees very well with the cross-sectional studies of 1.8 mm drop impacts on ZnS for the same velocity regime (5). The velocity dependence of three important features of the damage site: diameter of undeformed zone, maximum diameter damaged zone and maximum depth of crack, is shown in Figure 24. In these Figures the results for drop impacts on ZnS reported in (5) are also plotted. Taking into account that the jet used simulates an approximately 4 mm diameter diameter drop for most of this velocity range (see Figure 16) the agreement is quite good. As expected, the diameter of the undeformed zone for the jet impact is just over twice that for the drop, and the maximum diameter of cracking and maximum crack depth are greater.

Comparison of details of the damage zone as revealed by transmission and reflection microscopy (see Figures 20c and d, 21c and d, and 22c and d) reveals that the onset of cracking and that of jetting do not coincide. This observation is consistent with our ideas of the early stage of liquid/solid impact (2). The innermost cracks are closed without material removal. Cracks further outwards show material removal at the upraised edges. At the outermost cracks, again no material removal occurs (as shown in Figures 20a and b, 21a and b, and 22a and b). This is either due to the absence of "steps" across the cracks or due to lift-off of the jetting liquid. Maximum crack depth occurs not at the innermost boundary, but some way out. This is consistent with the build-up of the Rayleigh wave which initiates the cracks.

## SECTION 5

### MULTIPLE JET IMPACT ON SODA-LIME GLASS

#### 5.1 INTRODUCTION

The jet technique employed in this laboratory is an excellent way of studying the processes involved in rain erosion. The jet technique combined with the hydraulic bursting test is an inexpensive and efficient method of ranking new potential window materials (4).

In these tests the damage due to a single impact is measured. In the experiments to be described the impact damage due to multiple jet impact has been measured. The impact damage has been quantified using the hydraulic bursting test. Dynamic crack growth theories have been used to calculate the shape of the residual strength curves as a function of number of impacts. A good qualitative agreement between theoretical predictions and experimental results is obtained.

#### 5.2 EXPERIMENTAL

In these experiments, the newly adopted nozzle for 0.8 mm diameter jets has been used, which gives very reproducible impact damage over a wide velocity regime (1). The soda-lime-silica glasses were in the form of discs with a radius of 25 mm and an average thickness of 2.98 mm. The specimens were impacted in the as-received condition. The impacts were performed such that all the impacts were at the center of the specimen. Specimens were not dried in between two successive shots since the amount of water adhering to the specimen surface after impact was only small. Furthermore the "undried" surface will approach the in-flight conditions better. At least 10 specimens were used for each impact condition.

A new specimen holder was designed in which the specimens were held rigidly during impact. In this rig, the specimens are supported near the circumference. In some experiments the specimen was fully supported by and acoustically matched to a 25 mm thick glass disc. By comparing the impact damage for the two support conditions, the effects of stress wave reflections and bending stresses on the impact damage could be determined.

The impact damage was measured quantitatively using the hydraulic bursting technique described in an earlier report (1). The support ring with 20 mm radius was used to eliminate edge failures.

### 5.3 RESULTS

The various ways in which the data obtained can be analyzed are discussed in detail for the case of a single impact per specimen. The introduced concepts will be extended to clarify the "residual strength" curves for multiple impacts.

#### a. Single liquid jet impact

Specimens were subjected to a single central liquid jet impact travelling at a velocity in the range of 125 to 700 m s<sup>-1</sup>. Typical impact damage patterns are shown in Figure 25. The damage is comparable to that in zinc sulphide and consists of a central undamaged zone surrounded by short circumferential cracks. The density and the average size of these cracks increase with increasing impact velocity. At low impact velocities no impact damage could be detected.

The impact damage has been quantified using the hydraulic bursting technique. The results for single jet impact are shown in Figure 26. The figure shows that a certain critical impact velocity has to be reached before a reduction in the average fracture stress is observed. This velocity regime is followed by a transition region (150-300 m s<sup>-1</sup>) in which the average fracture stress decreases rapidly with increasing impact velocity. At high impact velocities, the average fracture stress is a much weaker function of the impact velocity.

At this stage, attention should be drawn to the bimodal distribution of the results in the transition region. For impact velocities between 150 and 300 m s<sup>-1</sup>, a wide scatter in the results is obtained. Some specimens have a low fracture stress while others have a fracture stress comparable to that for unimpacted specimens. The percentage of specimens with low fracture stress increases with impact velocity. To show these aspects the average fracture stresses for the two groups are plotted separately in Figure 27. The probability of failure due to impact damage as a function of impact velocity is plotted in Figure 28.

It should be stated explicitly that the observations of the jet impact process (13) using high-speed photography have shown that the variability of the results in the transition region is not caused by jet instabilities but is due to variations in the surface condition of the specimen.

The fracture stresses are converted to equivalent flow sizes (4) from which the fracture stress under different test conditions can be predicted. In general the equivalent flaw size,  $c$ , can be calculated from the fracture

stress,  $\sigma_f$ , and the critical stress intensity factor,  $K_{IC}$ , using

$$c = \frac{1}{\alpha} \left( \frac{K_{IC}}{\sigma_f} \right)^2 \quad (10)$$

where  $\alpha$  is a constant depending on the flaw and stress field geometry ( $\alpha$  ca. 2). The equivalent flaw sizes for single impacted specimens are shown in Figure 29 as a function of impact velocity. A good agreement between calculated and observed flaw sizes was found.

b. Multiple jet impact

The residual strength curves for double, triple, 5-fold and 10-fold impacts per specimen are shown in Figures 30a through d respectively. The residual strength curves for single and multiple impact are combined in Figure 31. The most salient features of this figure are the decrease in average fracture stress with increasing number of impacts and the reduction of the transition region. A typical example of the increase in impact damage with the number of impacts is shown in Figure 32. Not only do cracks grow due to subsequent impacts but also new cracks are formed. The deeply penetrating cracks are of a conical form. At high impact velocities or at a large number of impacts, the cone cracks intersect the rear surface creating a conical hole in the specimen (Figure 32f). This phenomenon which is clearly dependent upon the specimen geometry causes the plateau of minimum fracture stress at about 20 MPa in the residual strength curves.

The very low fracture stress obtained at double impact at  $700 \text{ m s}^{-1}$  is due to the formation of radial cracks emanating from the center of the rear surface. A combination of bending stresses and stress wave reflections provides the driving force for these cracks. Similar cracks are not observed under identical impact conditions on thick plates where the effect of reflected stress waves on the transient stress field responsible for the impact damage will be negligible. To show the increase in impact damage with number of impacts the fracture stresses for damaged specimens only are plotted in Figure 33. No statistically significant decrease in the average fracture stress of 'undamaged' specimens could be detected for the multiple impacted specimens. The failure probability curves plotted in Figure 34 show that the velocity region in which the fracture stress is bimodal is reduced considerably by multiple impact. It should be pointed out that the threshold velocity for impact damage seems to decrease only slowly with increasing number of impacts.

The equivalent flaw sizes, calculated according to equation 10, have been plotted in Figure 35. Generally a fair agreement with observed crack sizes was obtained.

c. The effect of stress wave reflection and specimen bending

In order to investigate the combined effect of stress wave reflection from the rear surface and bending stresses, single and double jet impact experiments were performed on specimens centrally supported by and acoustically matched to a 25 mm thick glass plate. The residual strength curves are shown in Figures 36 and 37 for single and double impacts per specimen respectively.

As can be expected, the effect of stress wave reflections and bending stresses on the residual strength is largest for high impact velocities. No effect could be detected at low impact velocities.

#### 5.4 DISCUSSION

In order to explain the observed phenomena, the impact process has to be considered in some detail. When a flat-ended cylindrical jet of radius  $r$  impacts a flat solid surface with a velocity  $V$ , the liquid initially behaves compressibly until stress waves generated at the circumference of the jet have reached the center of the jet (Figure 38). The pressure  $P$  during this stage of the impact is given by the "water-hammer" equation

$$P = \rho_w C_w V / (1 + \rho_w C_w / \rho_t C_t)$$

where  $\rho_w C_w$  and  $\rho_t C_t$  are the densities and appropriate shock wave velocities for the liquid and the target material respectively (43). The variation of shock wave velocity in water as a function of particle velocity has been tabulated in (44) and can be approximated for in the velocity range of interest by  $C_w = C_o + 2V$ , where  $C_o$  is the acoustic velocity for water of  $1500 \text{ m s}^{-1}$  (45,46). The duration of this pulse is for a cylindrical jet given by  $\tau = r/C_w$  (9,10). After the initial compressible stage of the impact, the pressure drops rapidly to the Bernouilli stagnation pressure  $P_i = \frac{1}{2}\rho V^2$  for the remainder of the impact. The ratio  $P/P_i = 2(C_o/V + 2)$  so that  $P_i$  only exceeds 10% of  $P$  for  $V \geq 500 \text{ m s}^{-1}$ . The impact damage will therefore be mainly due to the stress waves generated during the initial stage of the impact. The three types of stress waves generated are the shear, longitudinal, and Rayleigh surface waves. For impacts on an elastic half-space ca. 67% of the total

impact energy is contained in the Rayleigh wave (47). The interaction of the Rayleigh wave with surface discontinuities such as flaws can lead to flaw propagation and a reduction in the strength of a component (9,10,48). Recently we have attempted to measure with piezo-crystals the magnitude and time dependence of the Rayleigh surface waves produced by an impacting jet (49). The observations showed that the Rayleigh wave can be regarded as a triangular pulse in accordance with the pulse profile predicted in (50). The absolute magnitude of the pulse could however not be determined. An expression for the magnitude of the Rayleigh wave, using a quasi-static Hertzian analysis approach has been suggested(49);

$$\sigma_{\max} \propto \rho C V (1/R')^{\frac{1}{2}}$$

where  $r$  is the jet radius and  $R'$  the spatial coordinate normalized to the jet radius. For a given jet size, the approximation predicts an approximately linear relationship between pulse amplitude and impact velocity. With this estimate of the magnitude of the stress pulse, we can now consider the problem of crack growth due to single and multiple jet impact.

In the case of quasi static loading, the condition for crack growth (ignoring subcritical crack growth due to stress assisted chemical processes) is given by

$$K_{IC} = \alpha \sigma \sqrt{\pi a} \quad (11)$$

where the symbols have the same meaning as for equation 10. For the case of a crack subjected to a stress pulse, the dynamic stress intensity factor is initially also a function of time (51,52). For a stationary crack, the diffraction of the stress wave by a crack of finite dimensions leads to a damped oscillatory behavior of the stress intensity factor around the quasi-static value.

The stress intensity factor for a non-stationary crack has been analyzed (53-56). The stress intensity factor derived in (53) is particularly applicable to the problem of propagating small flaws and is given by

$$K = m \sigma (\pi a)^{\frac{1}{2}} (1 - v/v_{\max})^{\frac{1}{2}} U \quad (12)$$

where  $m$  is a geometrical constant,  $a$  the initial flaw size,  $v$  is crack velocity,  $v_m$  is the maximum crack velocity and  $U$  is given by the following series:

$$U = \sum_n \frac{1}{(2n-1)(2n+1)} \left\{ \frac{(2n+1)!}{2^{2n} n! n!} \right\}^2 \left( \frac{c-a}{a} \right)^n (-1)^{n+1}$$

where  $c$  is the current crack size.

Evaluation of this series indicates that for  $c < 20a$  (e.g., the range for which the analysis is applicable)  $U$  can be approximated by

$$U \approx \left\{ 1 + \frac{4}{5} \left( \frac{c-a}{a} \right) \right\}^{\frac{1}{2}} \quad (13)$$

It has been shown experimentally (57) that the dependence of the crack velocity on the dynamic stress-intensity factor is given by

$$v = v_{max} (1 - K_{IC}^2 / K^2) \quad (14)$$

where  $v_{max}$  is the maximum crack velocity.

With the analysis presented above we are now in a position to calculate the amount of crack growth due to a triangular stress pulse using a time iteration procedure (52).

Figure 39 shows the calculated crack growth in soda-lime glass as a function of the impact velocity normalized with respect to the threshold velocity. The pulse duration was taken as that for a 0.8 mm jet, e.g. 0.4  $\mu$ s. The initial flaw size was 20  $\mu$ m. Since the ratio of the residual to initial strength is proportional to  $(c_0/c)^{\frac{1}{2}}$  where  $c_0$  and  $c$  are the initial and post impact crack size respectively the normalized residual strength curve can be calculated as shown in Figure 40. In the analysis, all flaw statistical aspects of the impact damage problem are ignored. The calculated crack growth and residual strength curves must therefore be compared with the experimental results for impact damaged specimens only.

Considering all the approximations in the analysis, a good agreement between experimental and theoretical results is obtained. The same analysis can be used to calculate the effect of multiple impact on crack growth and residual strength. The results are shown in Figure 41. Once again an encouraging agreement between theoretical and experimental results is obtained.

The theory predicts that the transition region will be smaller with increasing number of impacts and (necessarily) a constant threshold velocity. These two features show up clearly from our experimental work.

## REFERENCES

1. Field, J.E., Matthewson, M.J. and van der Zwaag, S., annual report 1979 d, AFOSR-78-00125.
2. Field, J.E., Lesser, M.B., Davies, P.N.H., 1979, Proc. 5th Int. Conf. on Erosion by Liquid and Solid Impact (ELSI V), Cambridge, Paper 2.
3. Gorham, D.A. and Rickerby, D.G., 1975, J. Phys. E: Sci. Instrum., 8, 794.
4. Matthewson, M.J. and Field, J.E., 1980, J. Phys. E: Sci. Instrum., 13, 355.
5. Adler, W.F., 1979a, Effects Technology Int., Progress Report.
6. Adler, W.F., 1979b, Proc. 5th Int. Conf. on Erosion by Liquid and Solid Impact (ELSI V) Cambridge U.K., September 1979, Paper 9.
7. Brunton, J.H., 1959, Ph.D. Thesis, University of Cambridge.
8. Bowden, F.P. and Brunton, J.H., 1961, Proc. Roy. Soc., A263, 433.
9. Field, J.E., 1962, Ph.D. Thesis, University of Cambridge.
10. Bowden, F.P. and Field, J.E., 1964, Proc. Roy. Soc., A282, 331.
11. Fyall, A.A., 1967, Proc. 2nd Meersburg Conf. on Rain Erosion and Allied Phenomena.
12. Field, J.E., Camus, J.J., Gorham, D.A. and Rickerby, D.G., 1974, Proc. 4th Int. Conf. on Rain Erosion, Meersburg, W. Germany, p. 395.
13. Rickerby, D.G., 1977, PhD. Thesis, University of Cambridge.
14. Field, J.E., Gorham, D.A. and Rickerby, D.G., 1979a, ASTM Erosion Conf. Vail, Colorado 1977, ASTM, STP, 664 (ed. W.F. Adler), p. 298.
15. Gorham, D.A., Matthewson, J.M. and Field, J.E., 1979, ASTM Erosion Conf. Vail, Colorado 1977, ASTM, STP, 664 (ed. W.F. Adler), p. 320.
16. Field, J.E., Gorham, D.A., Hagan, J.T., Matthewson, J.M., Swain, M.V. and van der Zwaag, S., 1979b, Proc. 5th Int. Conf. on Erosion by Liquid and Solid Impact (ELSI V), Paper 13.
17. Lawn, B.R. and Swain, M.V., 1975, J. Mater. Sci., 10, 113.
18. Swain, M.V. and Hagan, J.T., 1976, J. Phys. D: Appl. Phys., 9, 2201.
19. Evans, A.G. and Wilshaw, T.R., 1976, Acta. Met., 24, 939.
20. Hagan, J.T. and Swain, M.V., 1978, J. Phys. D: Appl. Phys., 11, 2091.
21. Hagan, J.T., 1980, J. Mater. Sci., 15, 1417.
22. Lawn, B.R. and Evans, A.G., ibid, 1977, 12, 2195.
23. Lankford, J. and Davidson, D.L., ibid, 1979, 14, 1662 and 1669.
24. Shockley, D.A., Dao, K.C. and Curran, D.R., SRI Report PYU - 4928, Annual Report III, April 1979.
25. Dao, K.C., Shockley, D.A., Seaman, L., Curran, D.R. and Rowcliff, D.J., SRI Project PYU - 4928, Annual Report III, May 1979.
26. Naylor, M.A. and Page, T.F., Proc. 5th Int. Conf. on Erosion by Solid and Liquid Impact (ELSI V), Cambridge 1979, Paper 32.
27. Mulhearn, T.O., 1959, J. Mech. Phys. Sol., 7, 85.
28. Hertz, H., Hertz's Miscellaneous Papers, 1896, London: Macmillan, Chap. 5.

29. Nadai, A., *Plasticity*, (New York: McGraw-Hill), 1931.
30. Tabor, D., 1950, "Hardness of Metals", Clarendon Press, Oxford.
31. Smith, P.L. and Markin, J.E., 1965, *Phys. Letters*, 19, 541.
32. Evans, H.T. and McKnight, E.T., 1959, *Am. Mineralogist*, 44, 1210.
33. Mardix, S. and Brafman, O., 1967, *Acta Cryst.*, 23, 501.
34. Bither, T.A., Bouchard, R.J. and Cloud, W.H., 1968, *Inorg. Chem.*, 7, 2208.
35. Gillot, E., 1951, *Bull. Soc. Chim. France*, 39.
36. Lawn, B.R. and Fuller, E.R., 1975, *J. Mat. Sci.*, 10, 2016.
37. Shockley, D.A., Rowcliffe, D.J. and Dao, K.C., 1977, SRI publ., project 4938.
38. Williams, D.P. and Evans, A.G., 1973, *J. Test. Eval.*, 1, 264.
39. Schmitt, G., AFML, private communication.
40. Adler, W.F. and Hooker, S.V., 1978, *Wear*, 48, 103.
41. Shah, R.C. and Kobayashi, A.S., 1972, *ASTM Techn. Rep.* 513.
42. Hackworth, V., 1978, B.A.T. report AFML-TR-78-184.
43. de Haller, P., 1933, *Schweiz. Bauz.*, 101, 243.
44. Rice, M.H. and Walsh, J.M., 1957, *J. Chem. Phys.*, 26, 824.
45. Huang, Y.C., Hammitt, F.G. and Yang, W.J., 1973, *J. Fluids Eng.*, 276.
46. Heymann, F.J., 1968, *Trans. ASME, J. Basic Eng.*, 90, 400.
47. Miller, G. and Pursey, H., 1959, *Proc. Roy. Soc.*, A223, 521.
48. Field, J.E., 1966, *Phil. Trans. Roy. Soc. Lond.*, A260, 86.
49. Swain, M.V. and Hagan, J.T., 1980, *J. Mat. Sci.*, 15, 377.
50. Mooney, H.M., 1979, *Bull. Seis. Soc. Amer.*, 69, 473.
51. Sih, G.C., Embly, G.T. and Ravera, R.J., 1972, *Int. J. Solids and Structures*, 8, 977.
52. Freund, L.B., 1974, *J. Mech. Phys. Solids*, 20, 137.
53. Eshelby, J.D., in "Inelastic Behaviour of Solids", M.F. Kanninen (McGraw-Hill: New York 1970).
54. Broberg, K.B., 1960, *Ark. Fiz.*, 18, 159.
55. Achenbach, J.D. and Neusmen, R., 1971, *Int. J. Fract. Mech.*, 7, 77.
56. Rose, L.R.F., 1976, *Int. J. Fract. Mech.*, 12, 799.
57. Kerkhoff, F. and Richter, H., Proc. 2nd Conf. on Fracture, Brighton (1969).

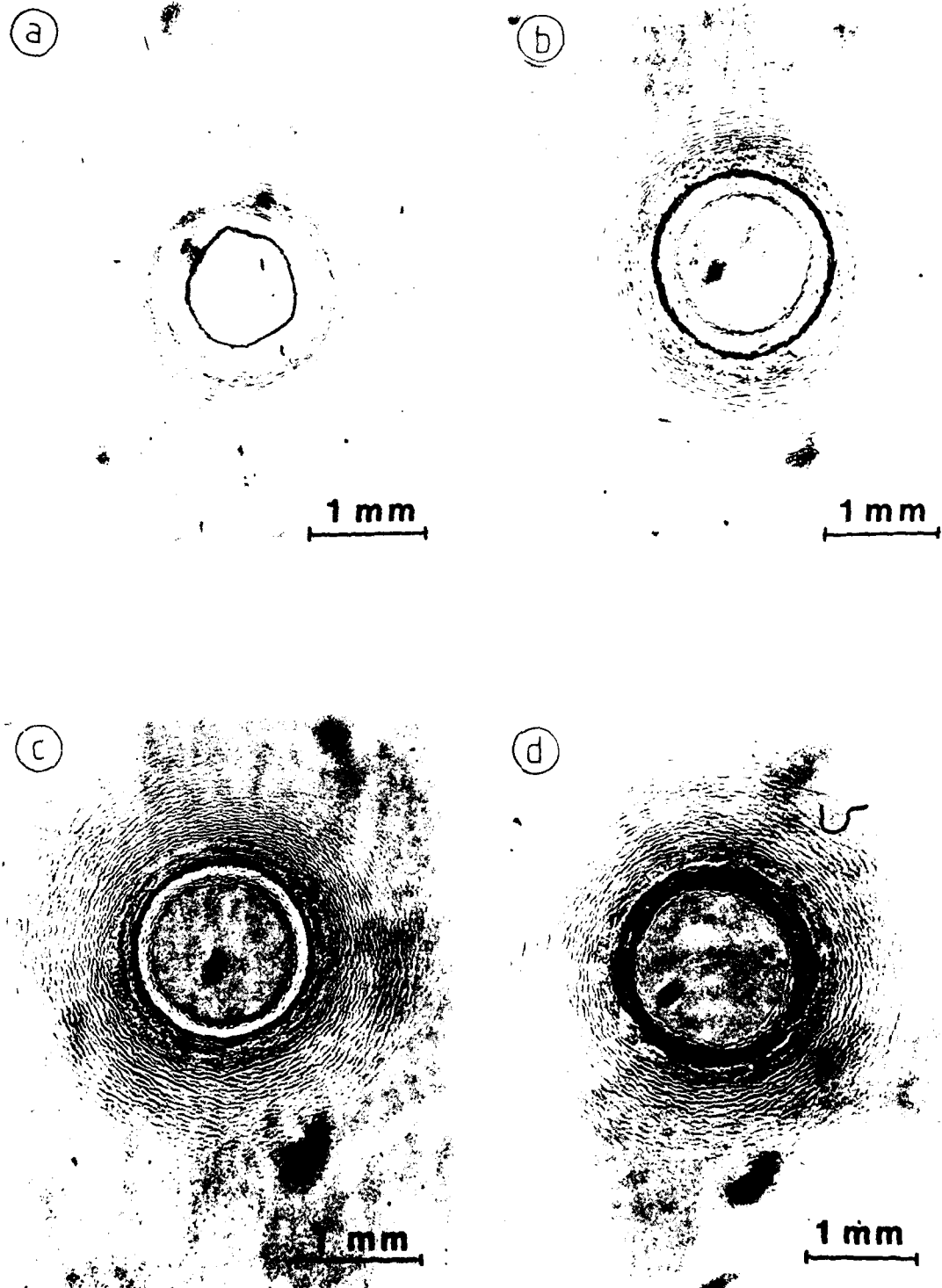


Figure 1.

Impact on PMMA by jets from a 0.4 mm orifice. (a)  $300 \text{ m s}^{-1}$  (b)  $400 \text{ m s}^{-1}$   
(c)  $500 \text{ m s}^{-1}$  (d)  $600 \text{ m s}^{-1}$

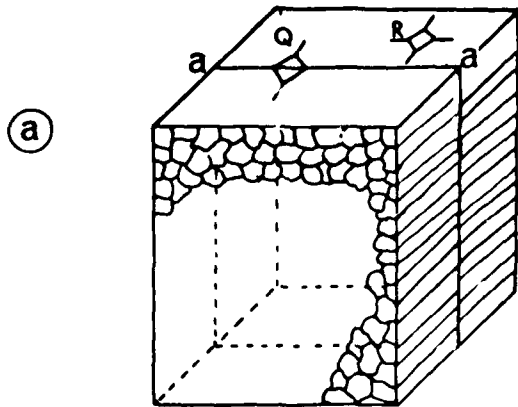
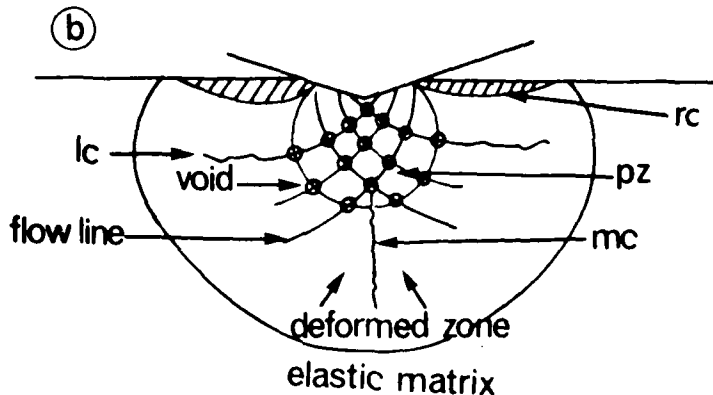
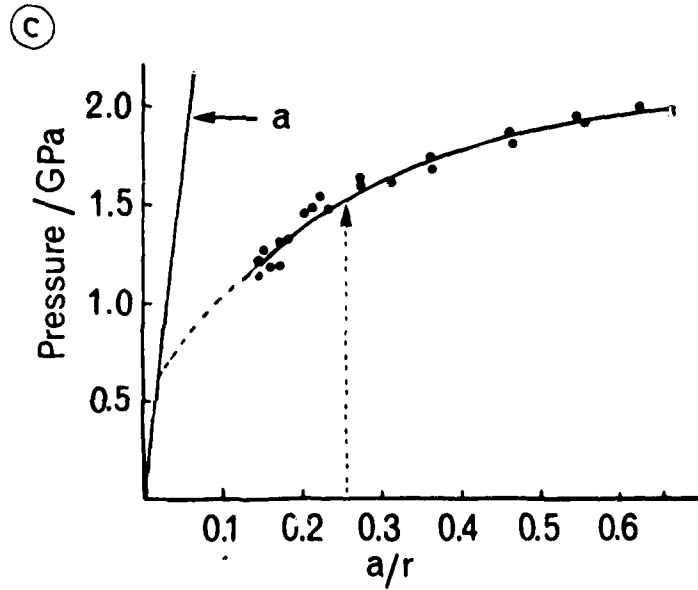


Figure 2.

- (a) A schematic diagram of the composite block illustrating the grain orientation and the indentations Q and R respectively along and away from the bulk interface.



- (b) A schematic diagram of flow lines in the porous zone, pz, and radial, median and lateral cracks, rc, mc and lc, respectively, within the deformed zone, dz.



- (c) Plot of the mean contact pressure as a function of the ratio of the contact radius to the sphere radius,  $a/R$ . The broken line is the elastic curve.



Figure 3.

- (a) and (b) show the surface damage around interface and bulk indentations, the interface is marked aa.
- (c) and (d) reveal grains a,b and c being pushed onto the specimen surface and the intergrannular nature of the dominant radial crack, rc. Both specimens were lightly etched.
- (e) Subsurface damage of an interface indentation revealing a heavily deformed zone, pz, and traces of median and lateral cracks within the plastic zone.

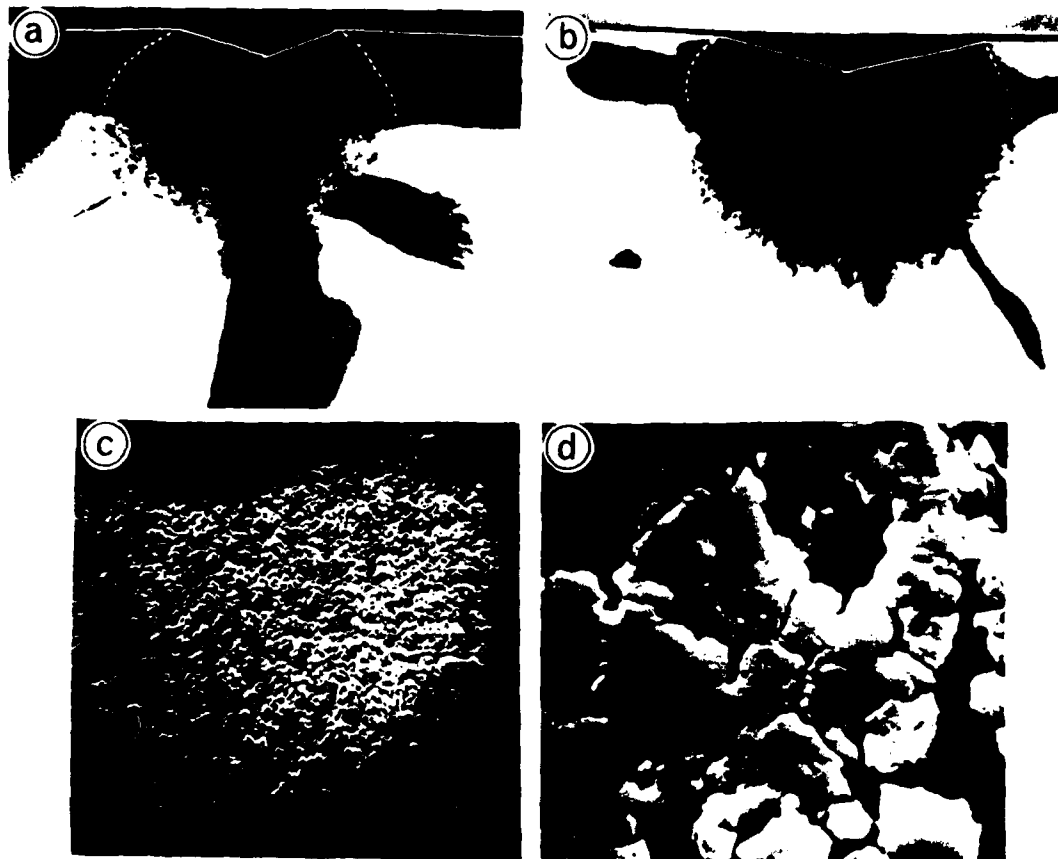


Figure 4.

- (a) and (b) are transmission optical micrographs of the heavily deformed zones, pz, around 150N interface and bulk indentations respectively. There are also traces of median, radial and lateral cracks.
- (c) and (d) are SEM micrographs at different magnifications of regions in (b) and they illustrate the porous nature of the heavily deformed zone, pz.

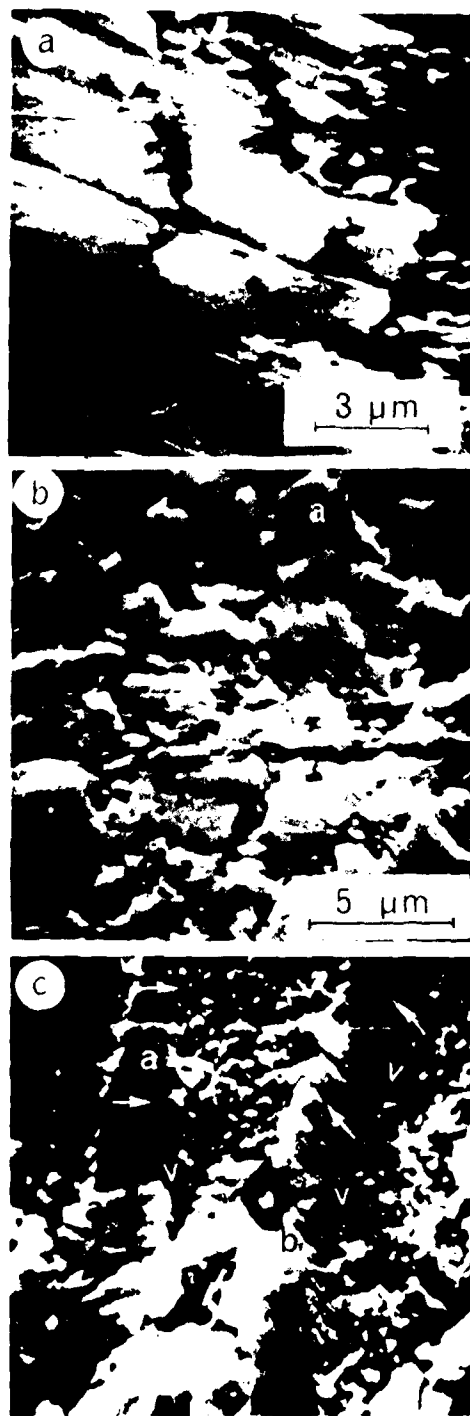


Figure 5.

(a) shows the displacement of fiducial line, ff, across the grain boundaries and (b) and (c) show deformation within the grains themselves. The orientation of the grains in (b) is as illustrated in Figure 1(a), while the loading axis in (c) was parallel to the long axis of the grains.

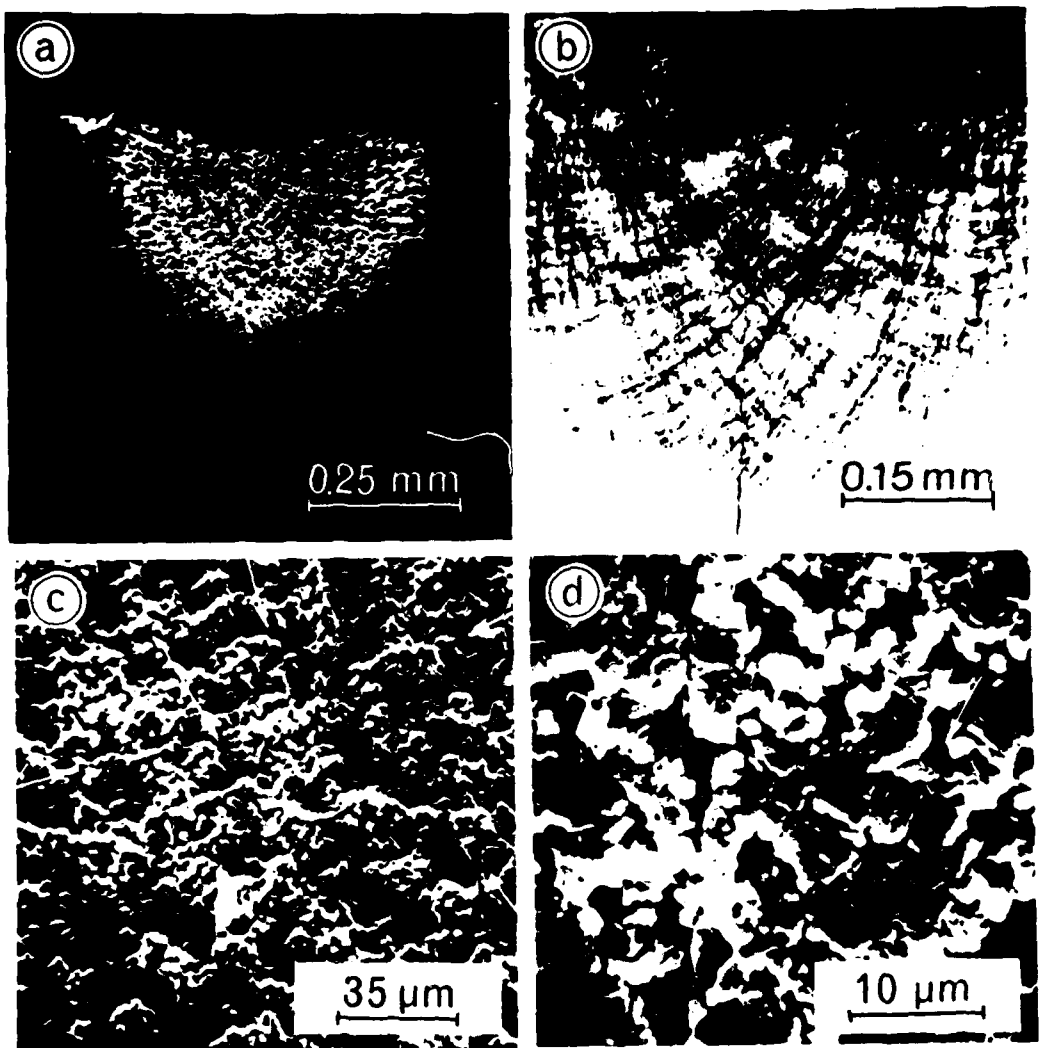


Figure 6.

(a) and (b) illustrate the spiral flow lines in the porous zone for the larger and smaller grain size material; (c) and (d) are higher magnifications of (a) and (d) show the high void density along the flow lines.

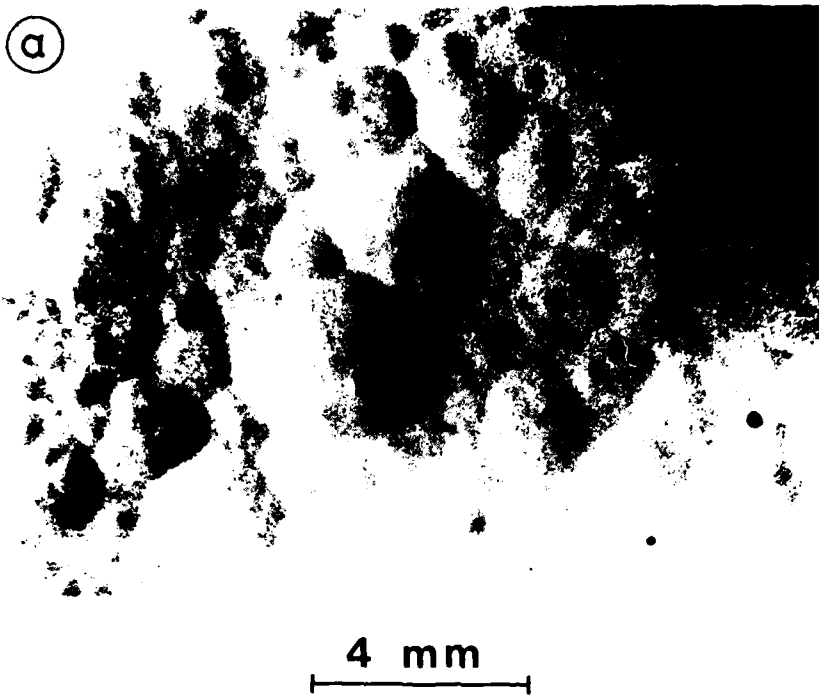


Figure 7.

- a The "pebble structure" below the surface.
- b etched cross-section of the specimen, revealing columnar grains  
( $2 \times 2 \times 25 \mu\text{m}$ ).

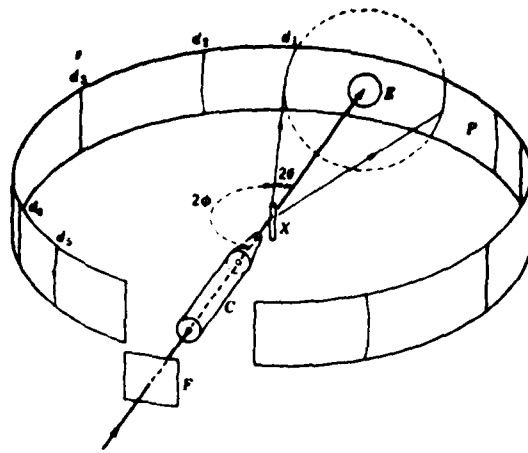


Figure 8. Diagram of the Debye-Scherrer technique.

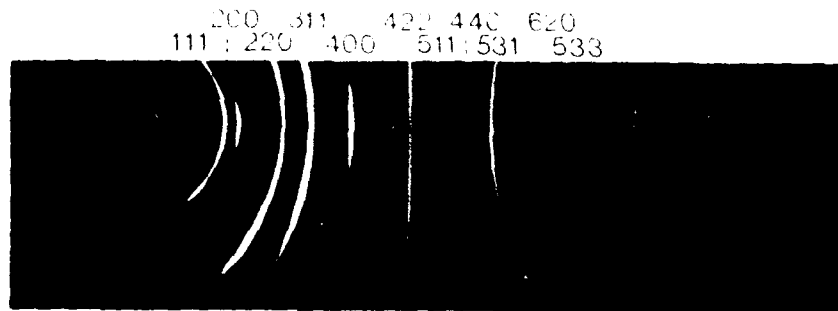


Figure 9. Debye-Scherrer pattern with corresponding lattice parameters for CVD zinc sulphide. The pattern observed is that for the zinc blende or sphalerite structure.

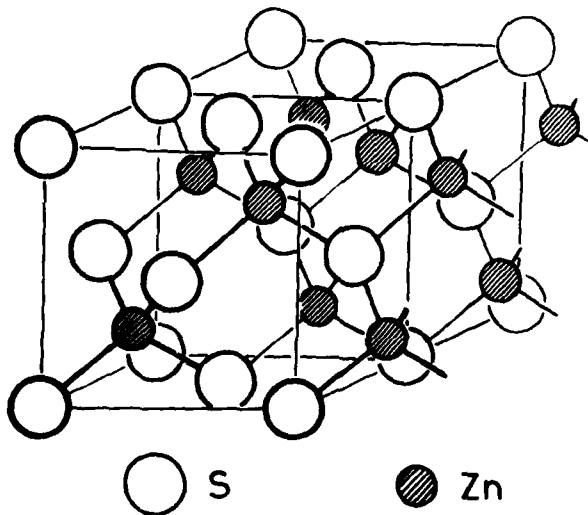


Figure 10. Zinc blende or sphalerite structure. This structure is closely related to that of diamond.

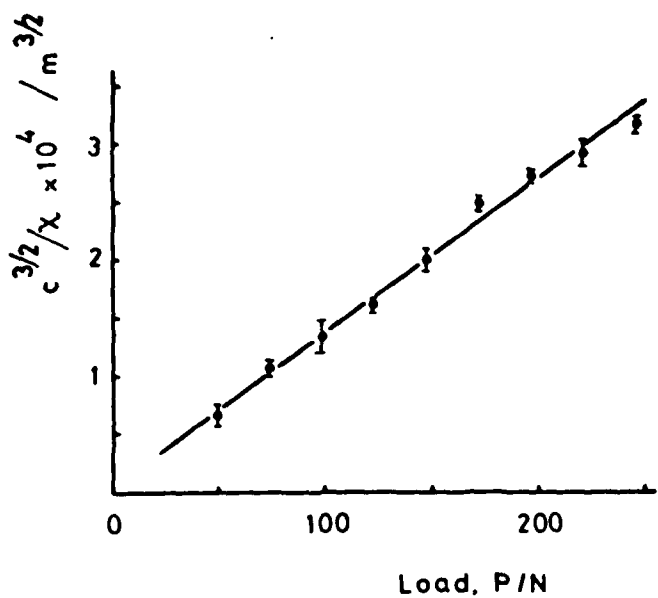


Figure 11. Plot of load versus  $(\text{crack length})^{3/2}$  for ZnS. The inverse of the slope of the line gives a critical stress concentration factor  $K_{IC} = 0.75 \text{ MPa m}^{1/2}$ .

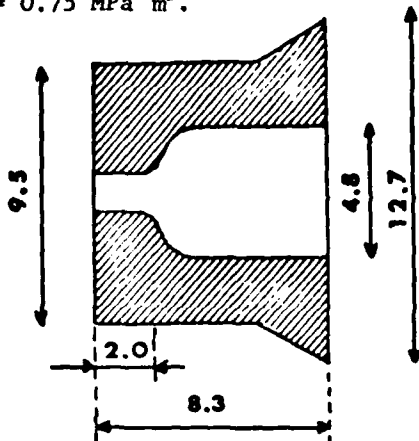


Figure 12. Diagram of nozzle with curved transition between chamber and orifice. Diameter of orifice was 0.8 mm.

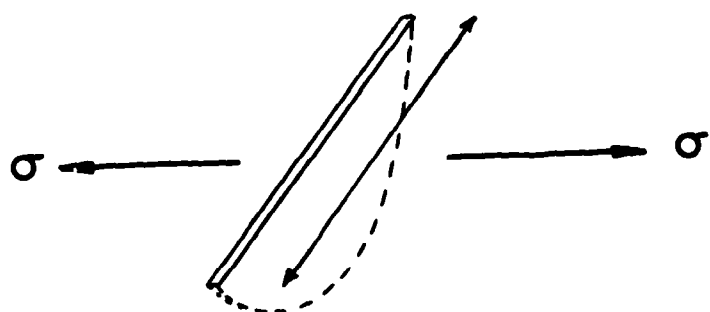


Figure 13. Semi-elliptical flaw in unidirectional stress field.

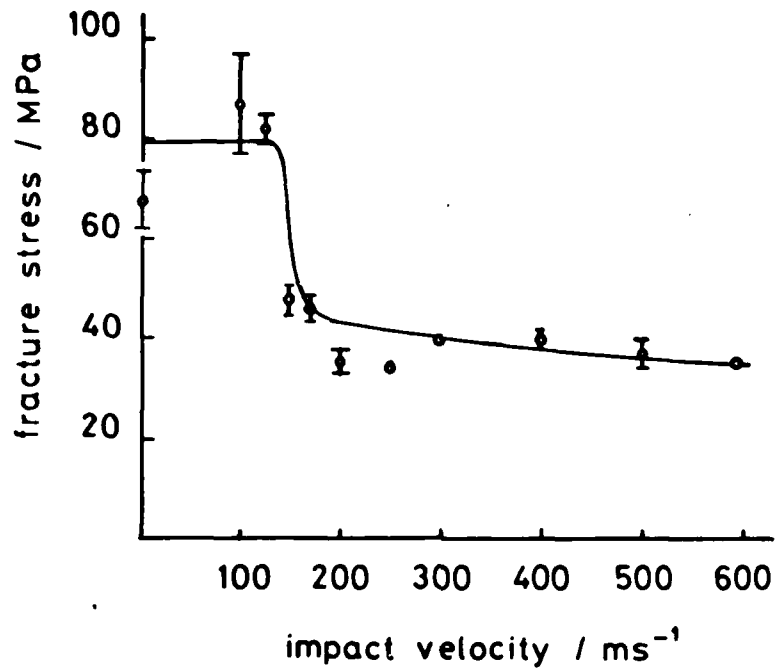


Figure 14. "Residual strength" curve for zinc sulphide for impacts with 0.8 mm diameter jets.

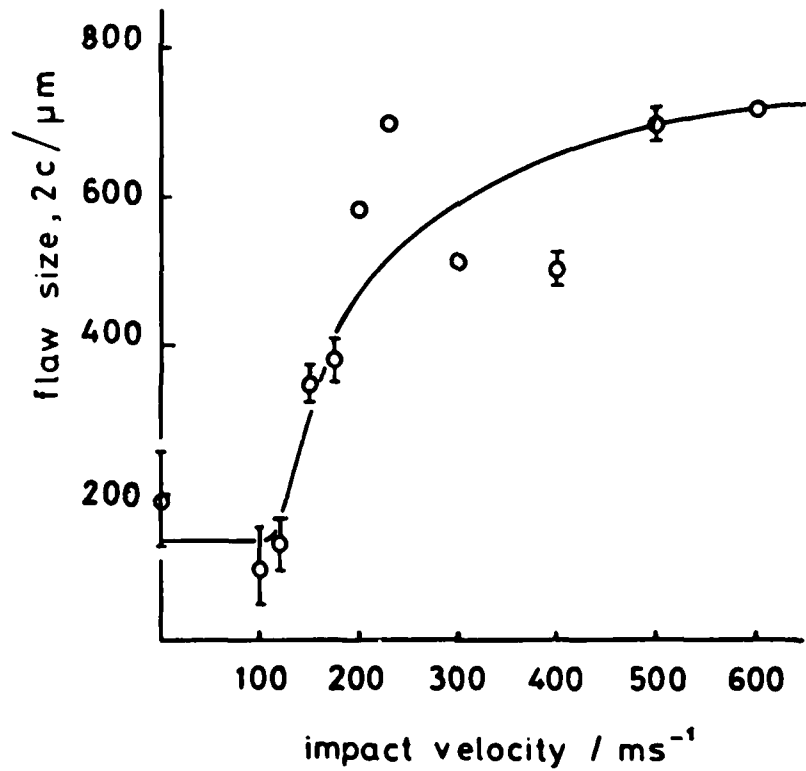


Figure 15. Equivalent flaw sizes for zinc sulphide as function of impact velocity.

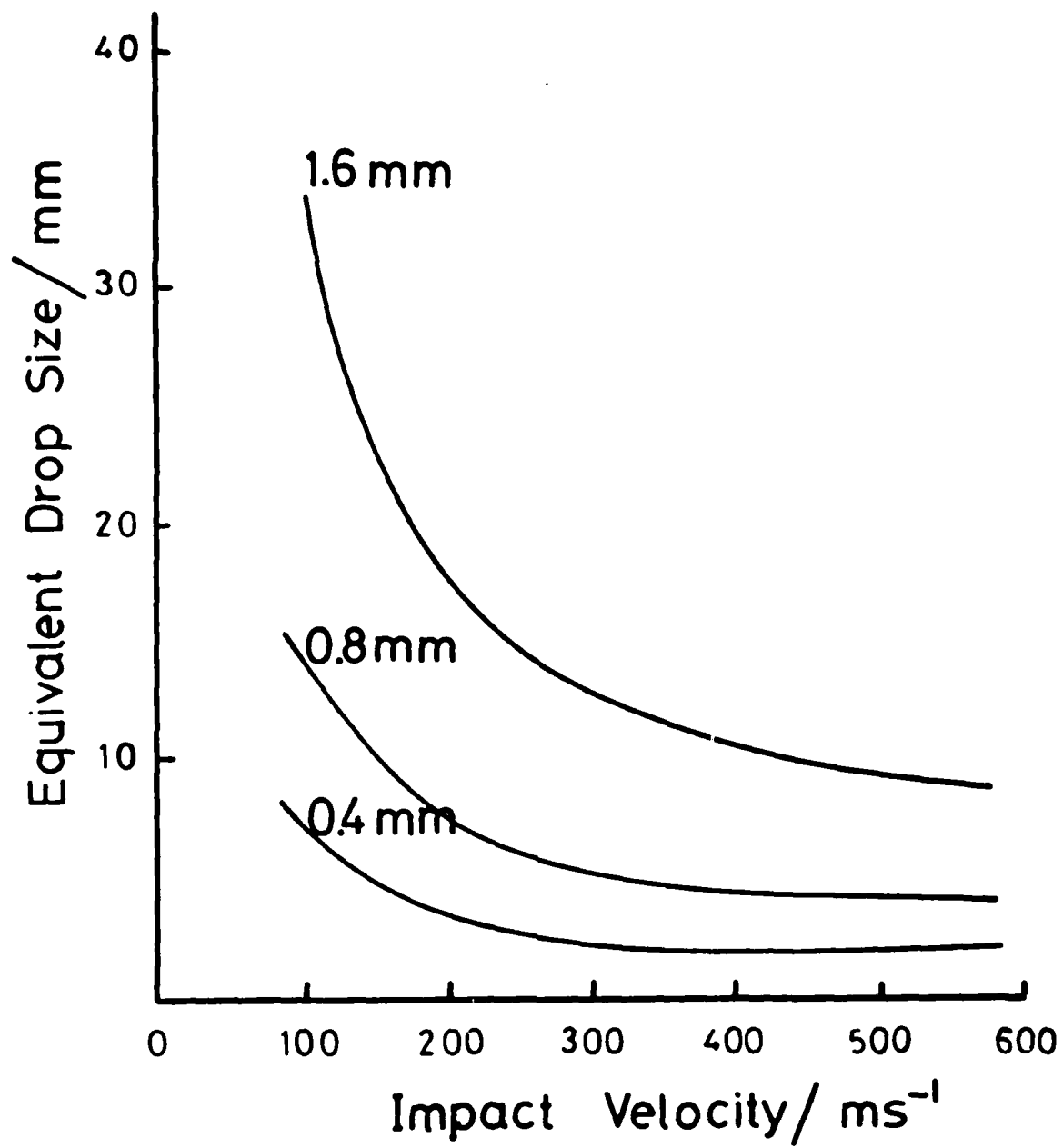


Figure 16. Equivalent drop sizes for several nozzle diameters.

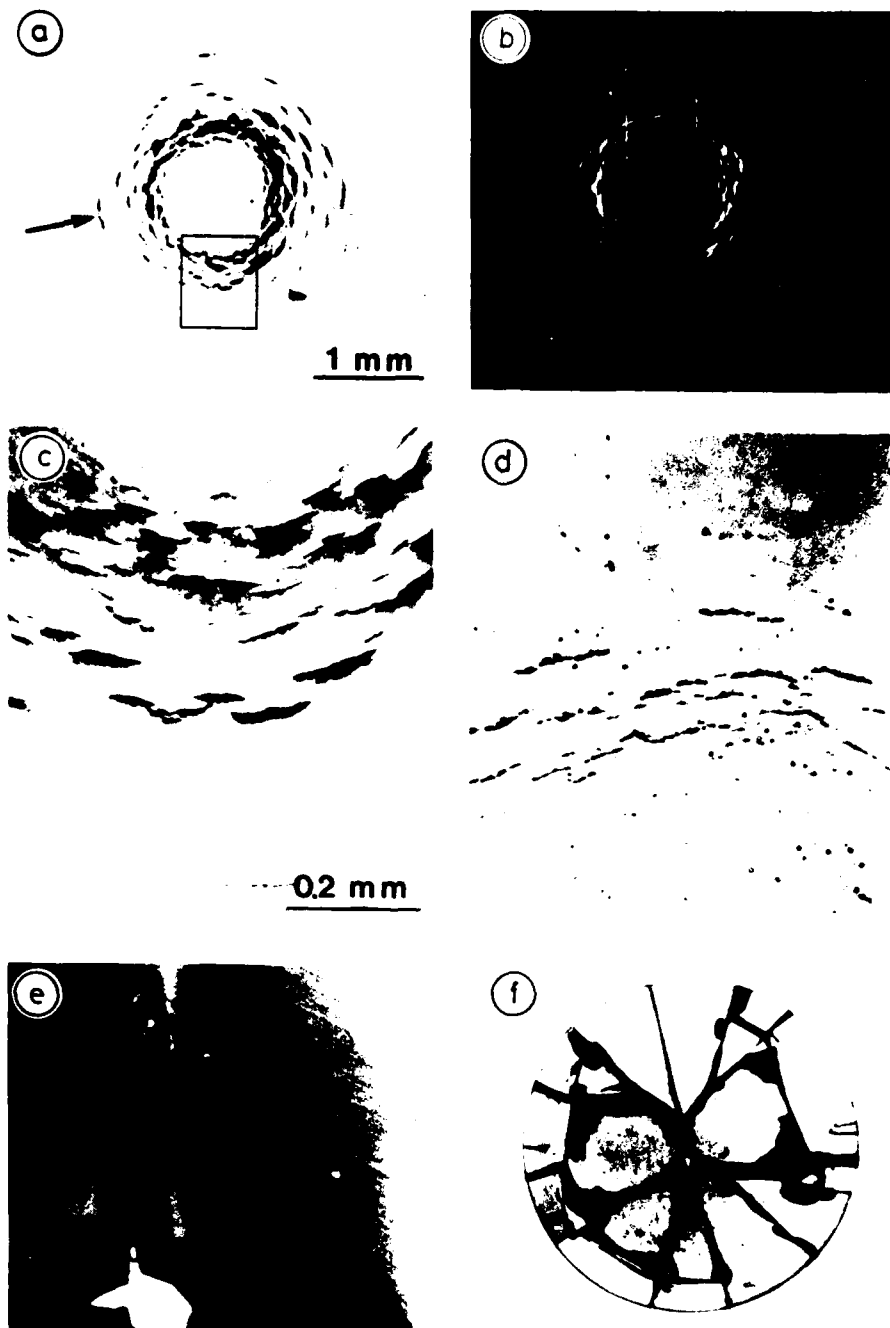


Figure 17. 0.8 mm jet impact at  $175 \text{ m s}^{-1}$  on ZnS.

- a is a optical transmission micrograph of the impact damage. The flaw leading to failure in the pressure tester is arrowed.
- b is a micrograph for oblique reflective illumination (magnification as in a).
- c and d are enlargements of the areas marked in a and b respectively (magnification of d as for c).
- e and f show the specimen after failure in the pressure tester.

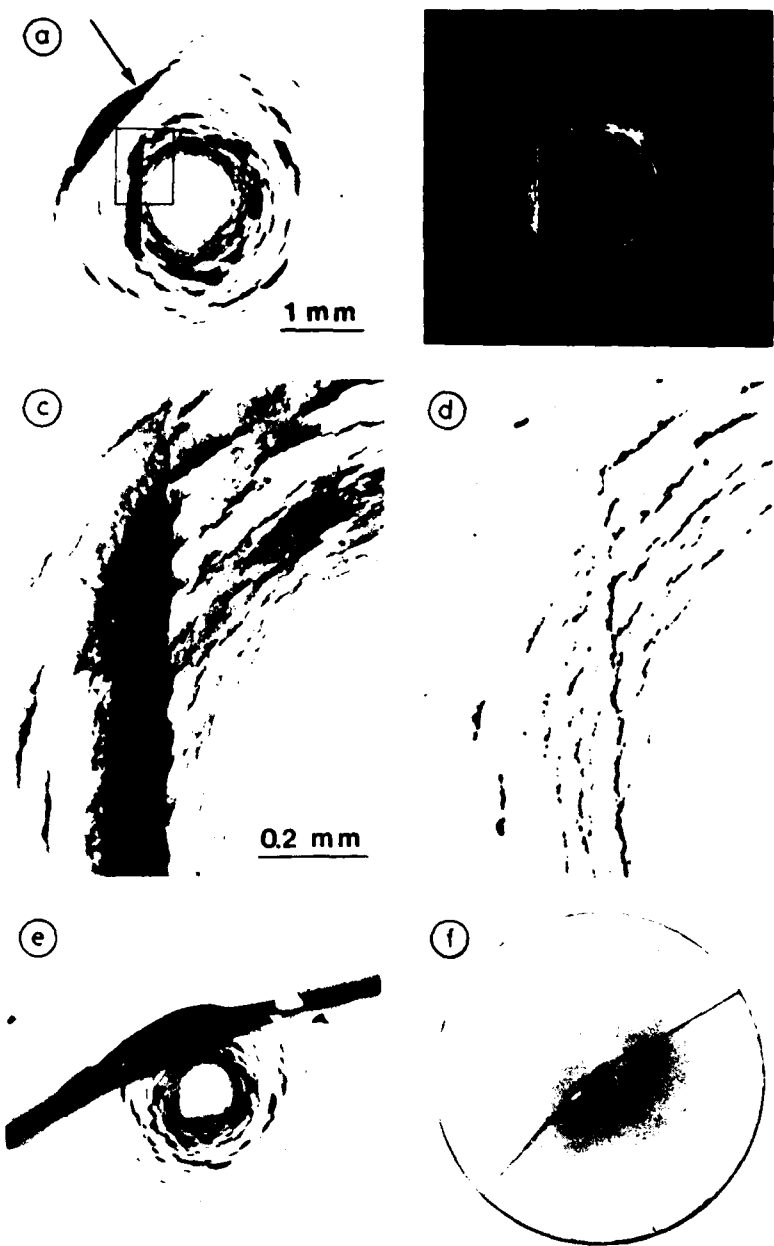


Figure 18. 0.8 mm jet impact at  $200 \text{ m s}^{-1}$  on ZnS.

- a is an optical transmission micrograph of the impact damage. The flaw leading to failure in the pressure tester is arrowed.
- b is a micrograph for oblique reflective illumination (magnification as in a).
- c and d are enlargements of the areas marked in a and b respectively (magnification of d as for c).
- e and f show the specimen after failure in the pressure tester.

(a)



1 mm

(b)

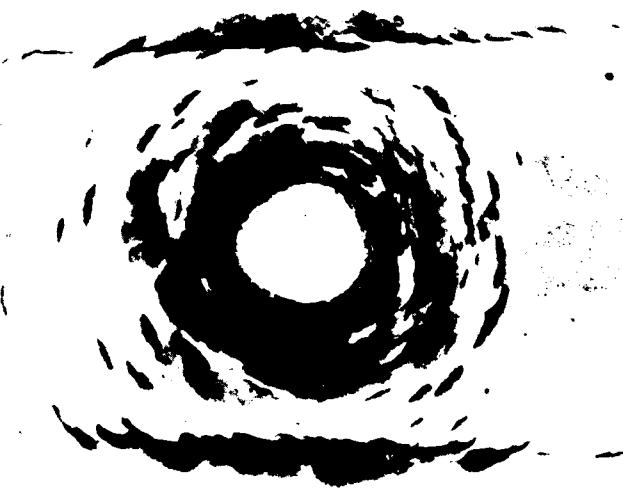


Figure 19. 0.4 mm jet impact at  $400 \text{ m s}^{-1}$  and  $500 \text{ m s}^{-1}$  on zinc-rich zinc sulphide leading to the propagation of residual grinding marks.

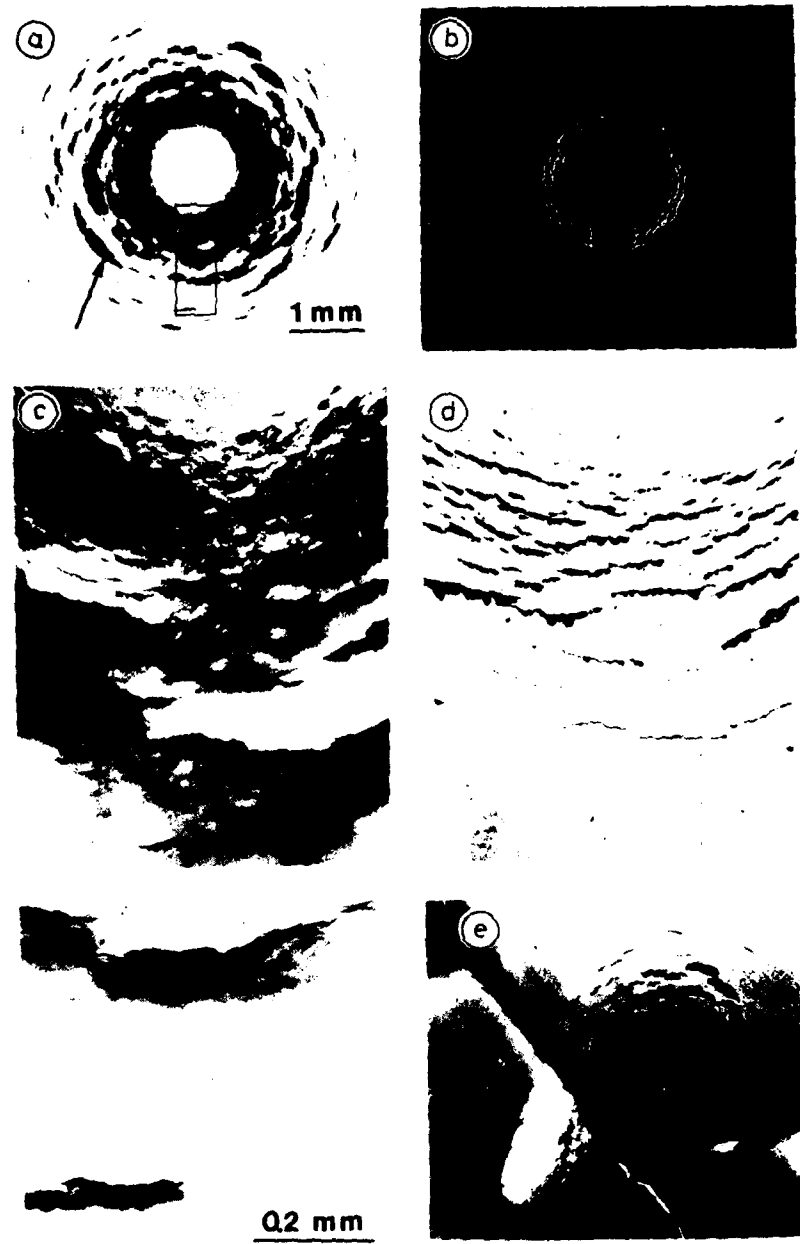


Figure 20. 0.8 mm jet impact at  $300 \text{ m s}^{-1}$  on ZnS.

a is an optical transmission micrograph of the impact damage. The flaw leading to failure in the pressure tester is arrowed.

b is a micrograph for oblique reflective illumination (magnification as in a).

c and d are enlargements of the areas marked in a and b respectively (magnification of d as for c).

e shows the specimen after failure in the pressure tester.

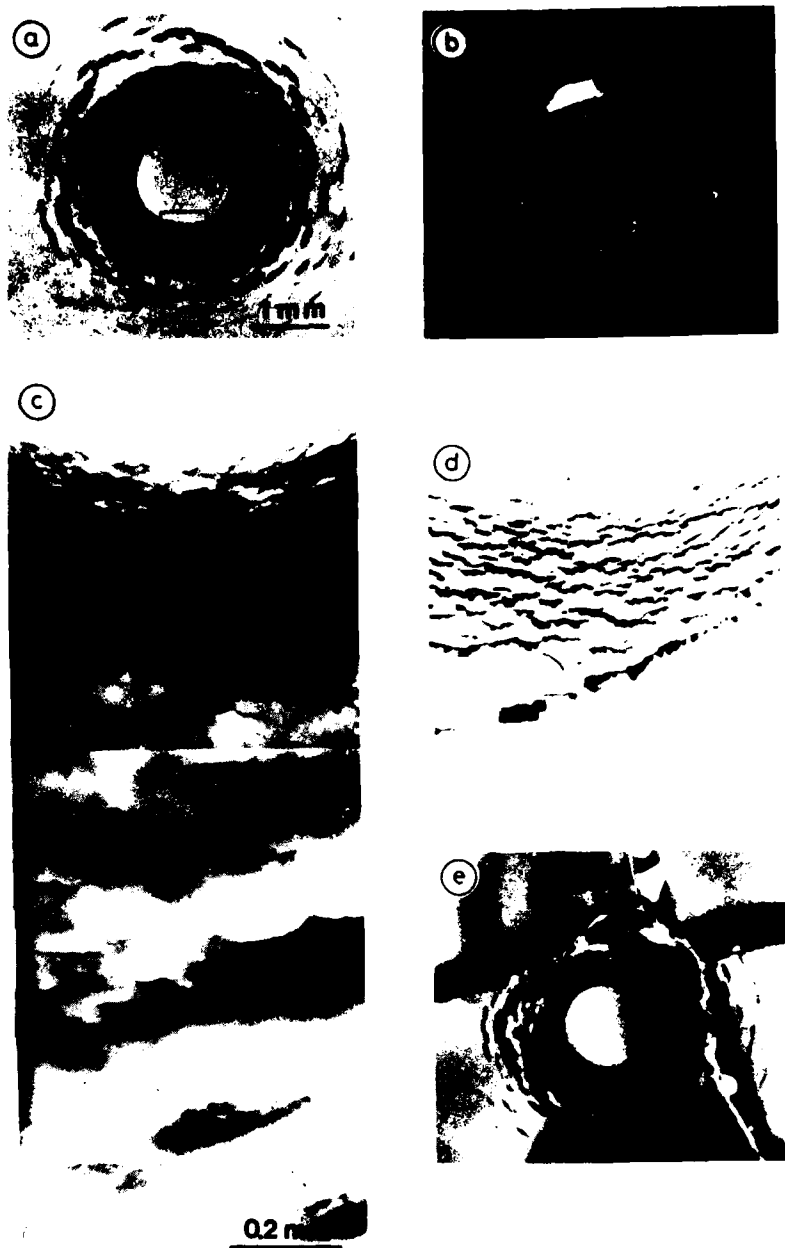


Figure 21. 0.8 mm jet impact at  $500 \text{ m s}^{-1}$  on ZnS.

- a is an optical transmission micrograph of the impact damage. The flaw leading to failure in the pressure tester is arrowed.
- b is a micrograph for oblique reflective illumination (magnification as in a).
- c and d are enlargements of the areas marked in a and b respectively (magnification of d as for c).
- e shows the specimen after failure in the pressure tester.

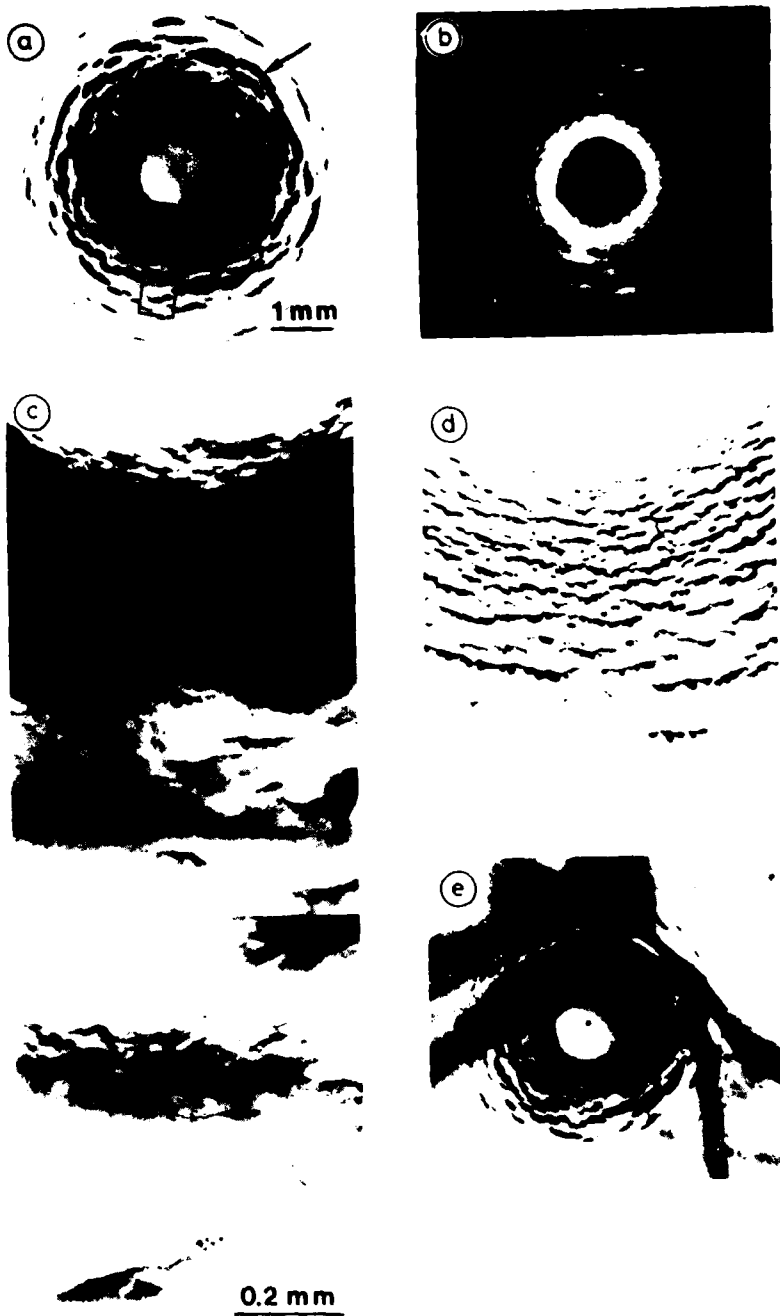


Figure 22.  $0.8 \text{ mm}$  jet impact at  $600 \text{ m s}^{-1}$  on  $\text{ZnS}$ .

- a is an optical transmission micrograph of the impact damage. The flaw leading to failure in the pressure tester is arrowed.
- b is a micrograph for oblique reflective illumination (magnification as in a).
- c and d are enlargements of the areas marked in a and b respectively (magnification of d as for c).
- e shows the specimen after failure in the pressure tester.

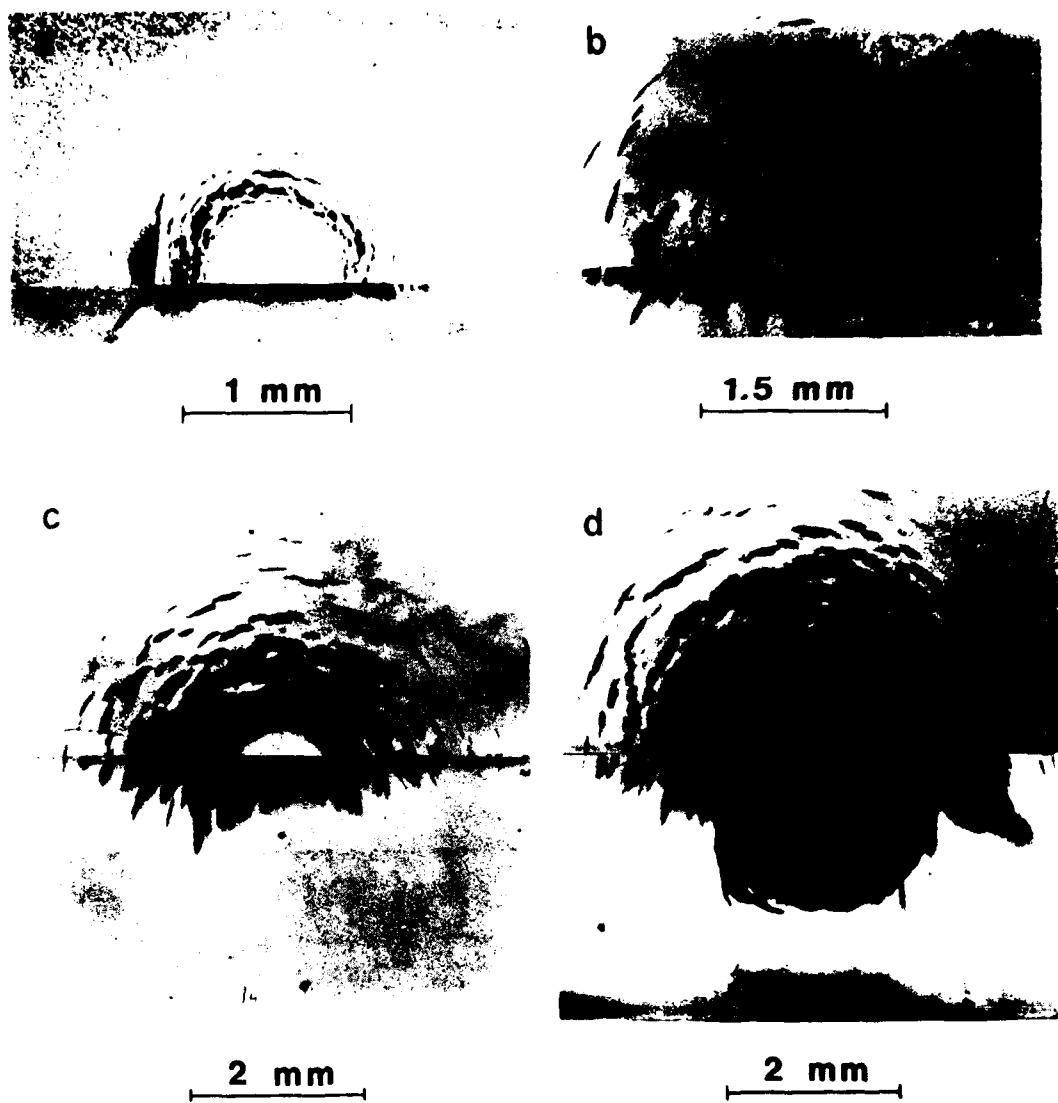


Figure 23. cross-sections of 0.8 mm jet impacts

- a     $175 \text{ m s}^{-1}$
- b     $300 \text{ m s}^{-1}$
- c     $400 \text{ m s}^{-1}$
- d     $600 \text{ m s}^{-1}$

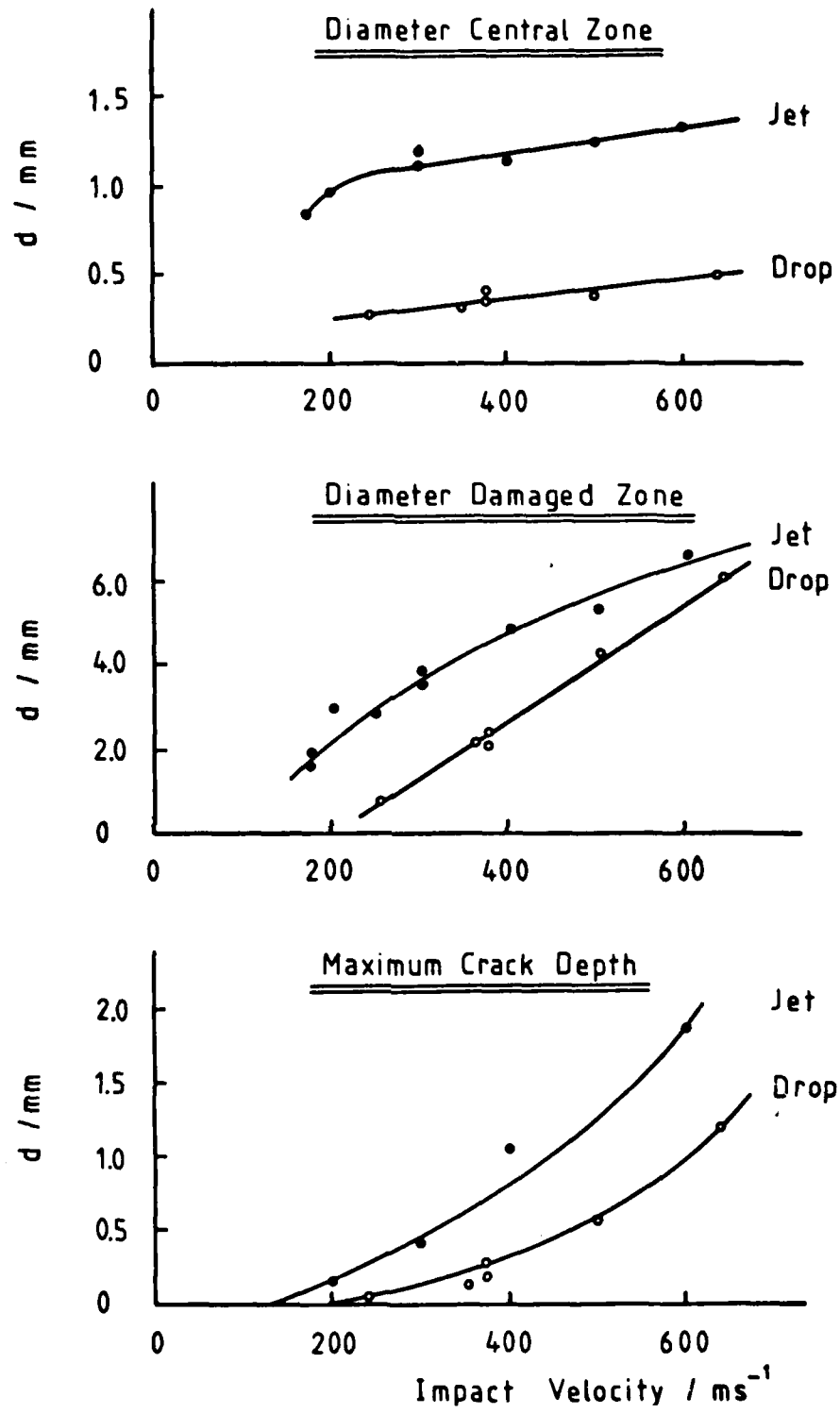


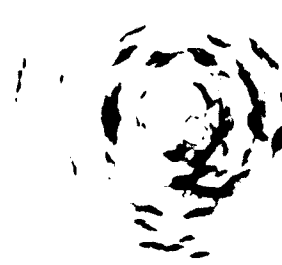
Figure 24. Velocity dependence of damage parameters.

- a diameter of undeformed zone
- b maximum diameter of damaged zone
- c maximum crack depth.

(a)



(b)



(c)



1 mm

Figure 25. 0.8 mm jet impact damage on soda-lime-silica glasses (a)  $225 \text{ m s}^{-1}$  (b)  $300 \text{ m s}^{-1}$  and (c)  $600 \text{ m s}^{-1}$ .

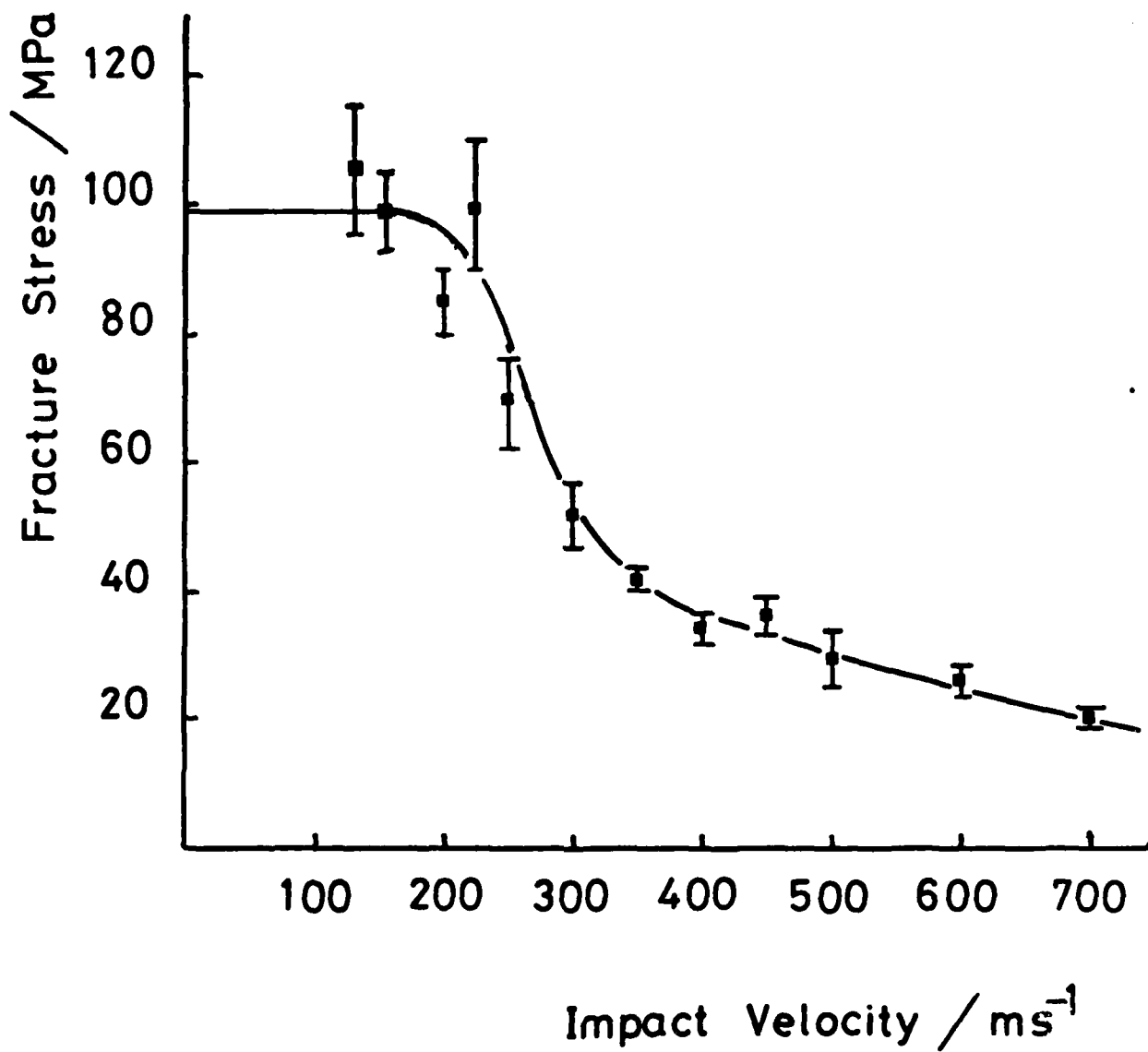


Figure 26. Residual strength curve for single 0.8 mm jet impact on soda-lime-silica glass.

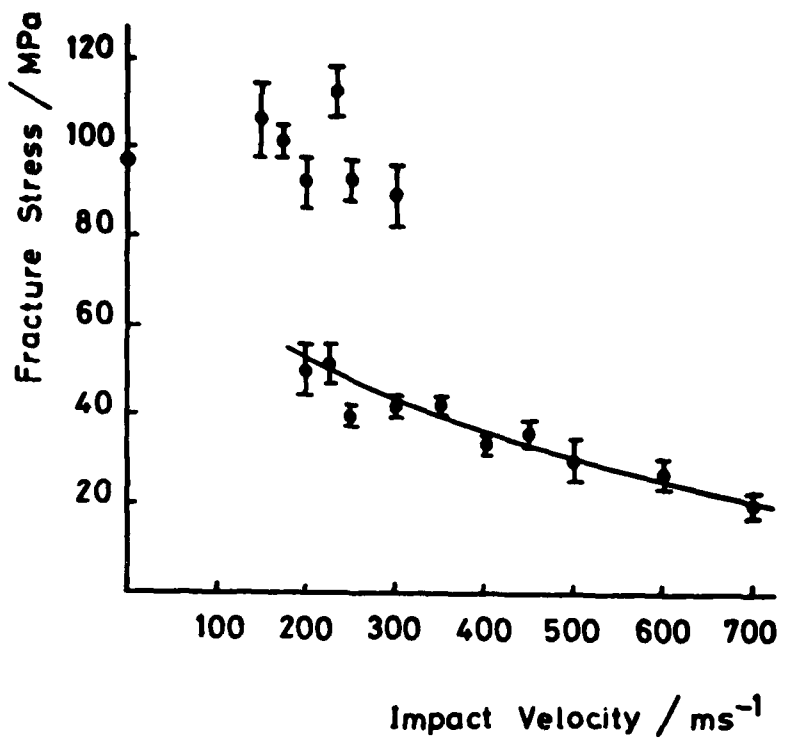


Figure 27. as Figure 26. Data are now plotted separately for "damaged" and "undamaged" specimens.

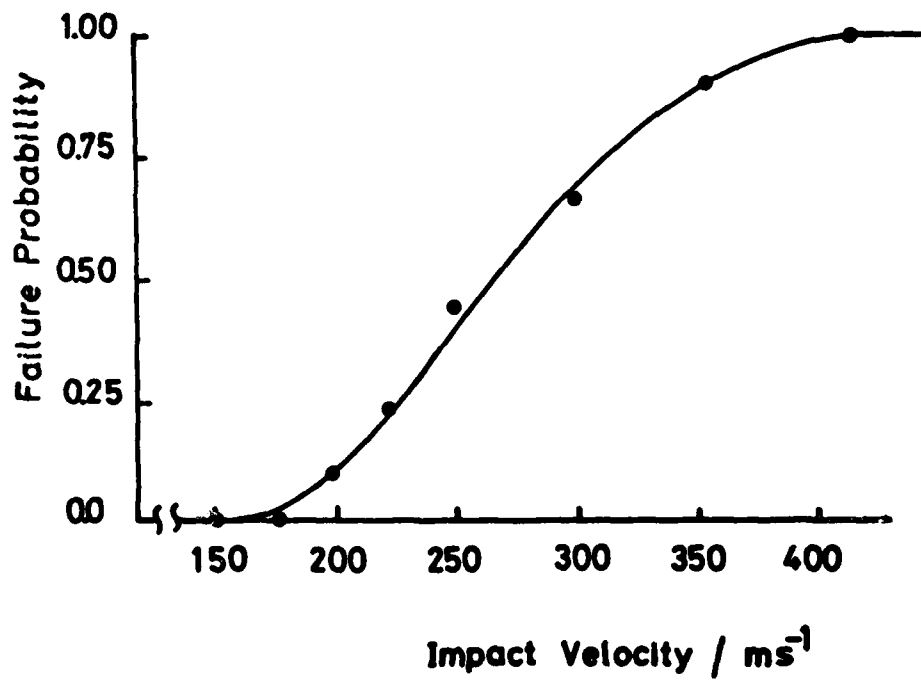


Figure 28. Probability of failure due to single 0.8 mm jet impact.

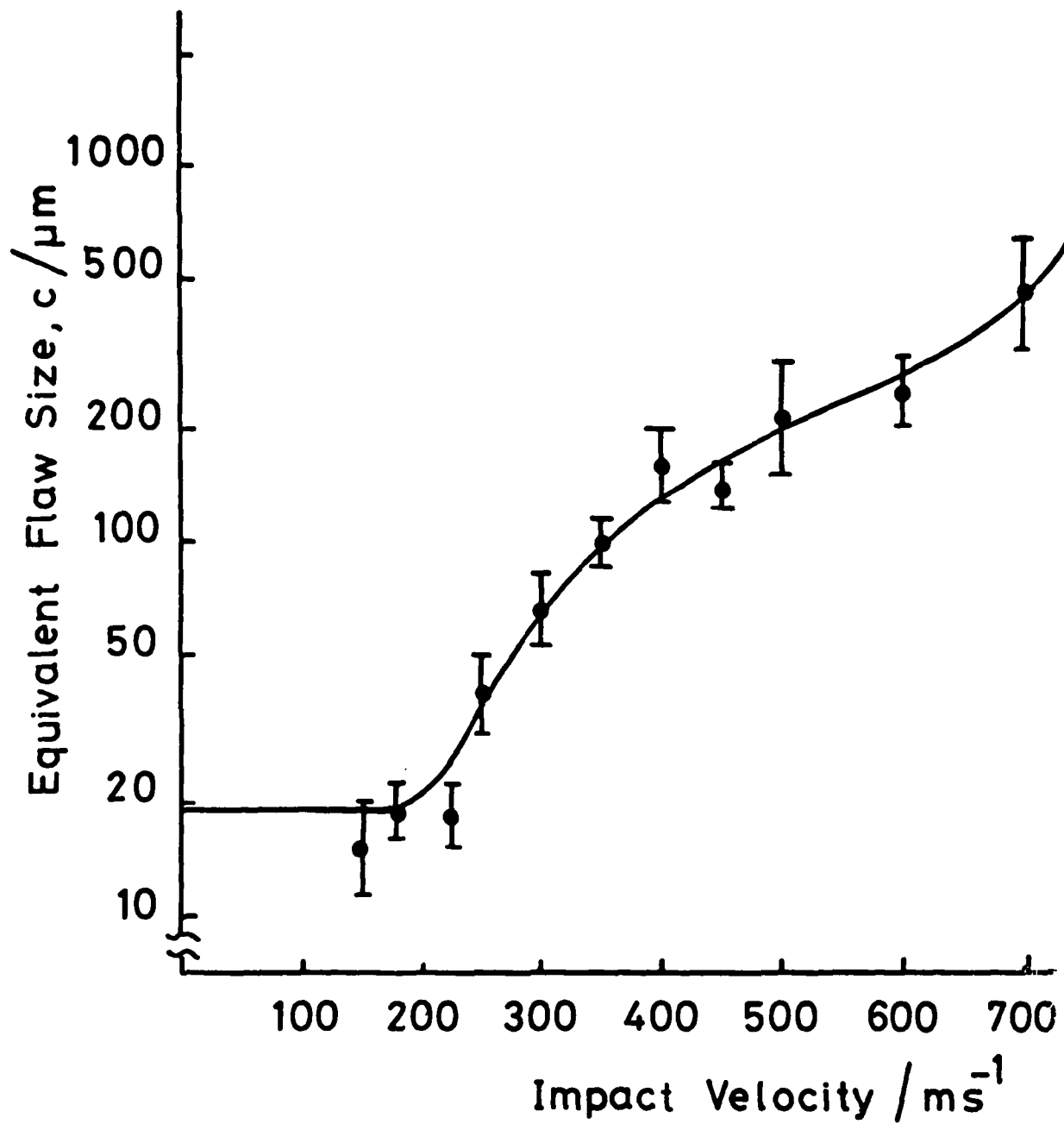
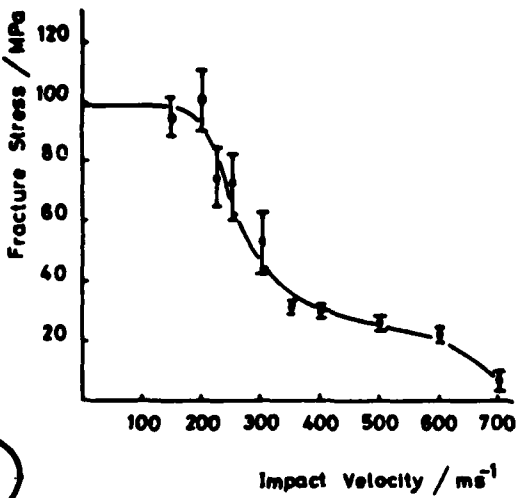
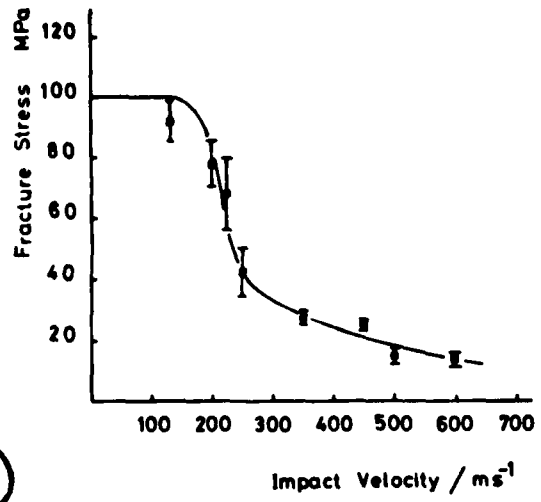


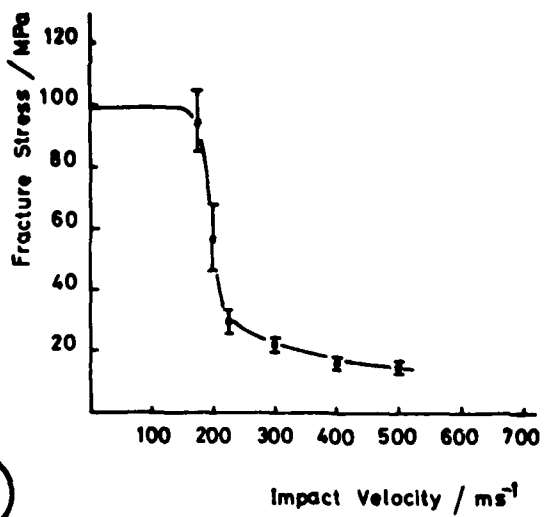
Figure 29. Results of Figure 26 replotted in terms of equivalent flaw size.



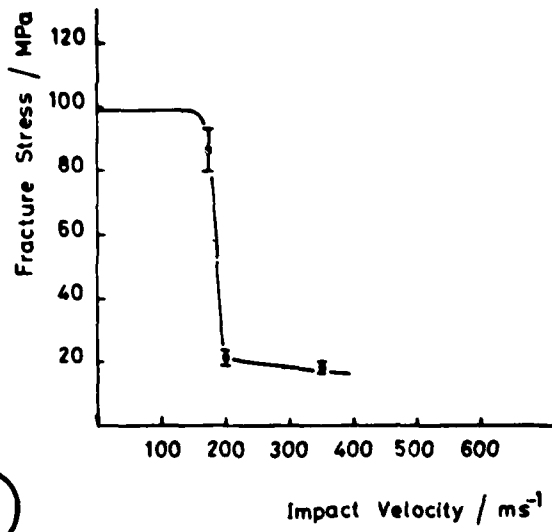
(a)



(b)



(c)



(d)

**Figure 30.** Residual strength curves for multiple 0.8 mm jet impact on soda-lime-silica glass. (a) double (b) triple (c) 5-fold and (d) 10-fold impact per specimen.

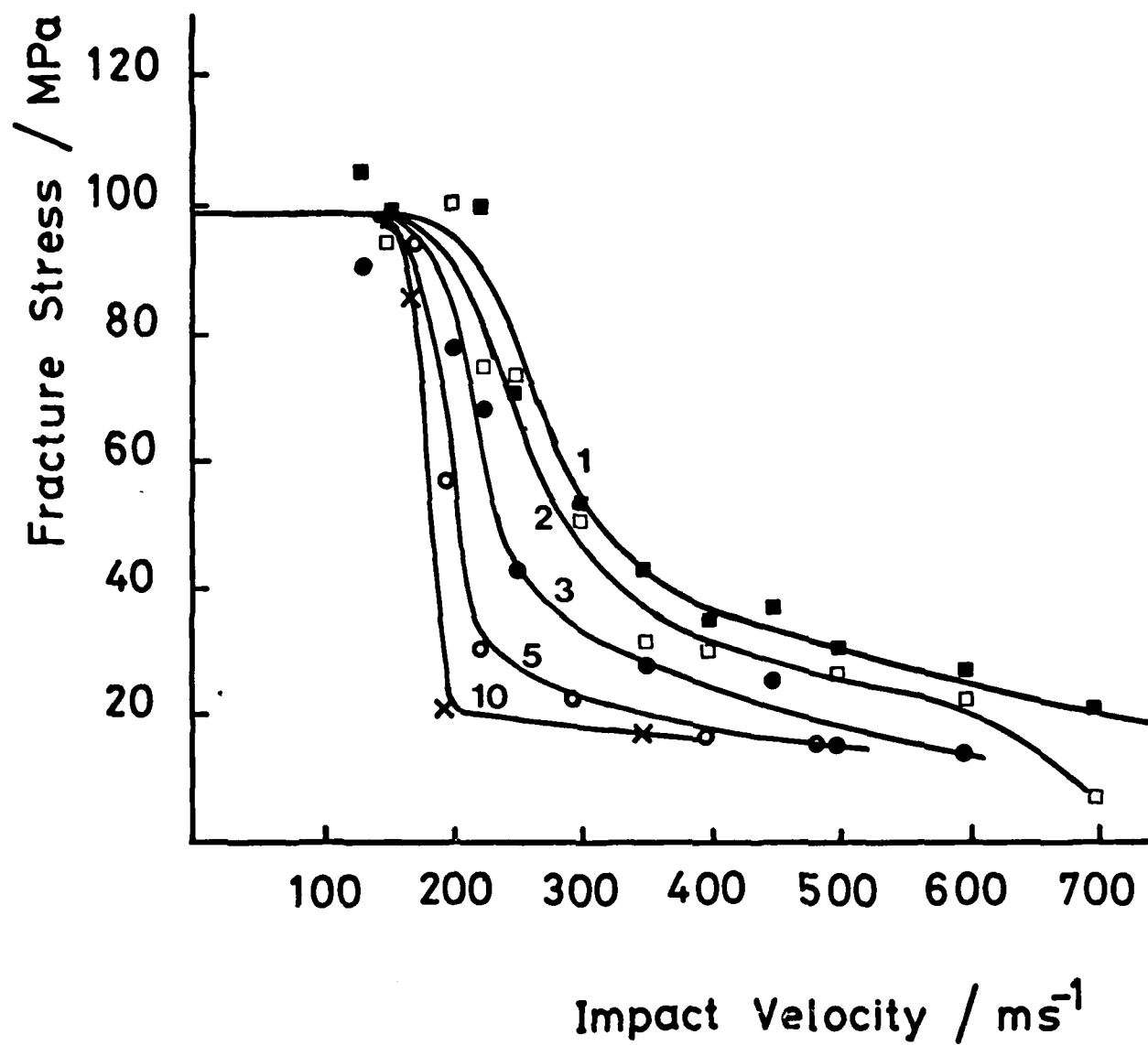
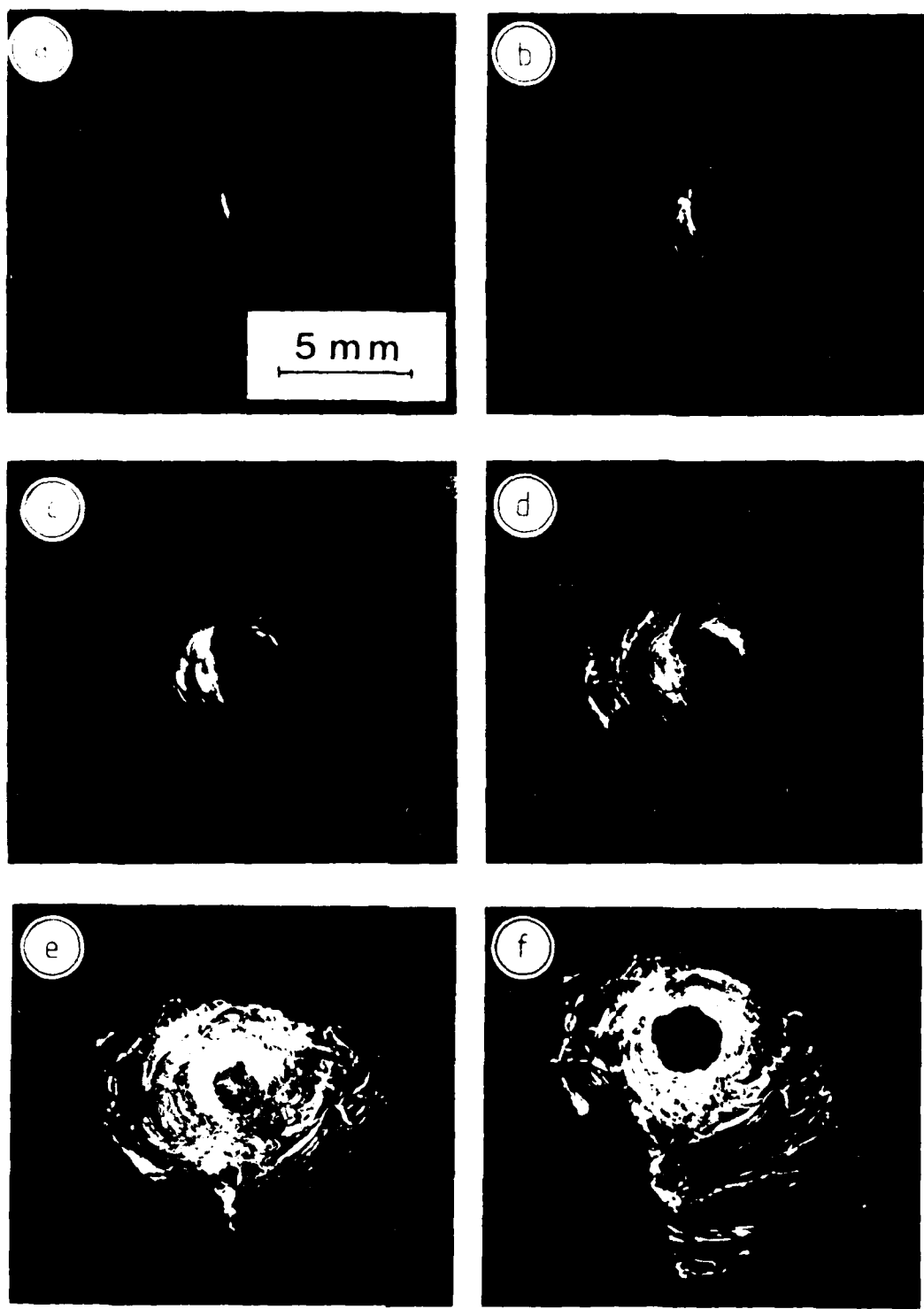


Figure 31. Residual strength curves for single and multiple 0.8 mm jet impact.



**Figure 32.** A typical example of the increase of impact damage with number of impacts for a 0.8 mm jet at 250 m s<sup>-1</sup>.  
(a) after 2 impacts                   (b) after 3 impacts  
(c) after 5 impacts                   (d) after 8 impacts  
(e) after 15 impacts                   (f) after 23 impacts

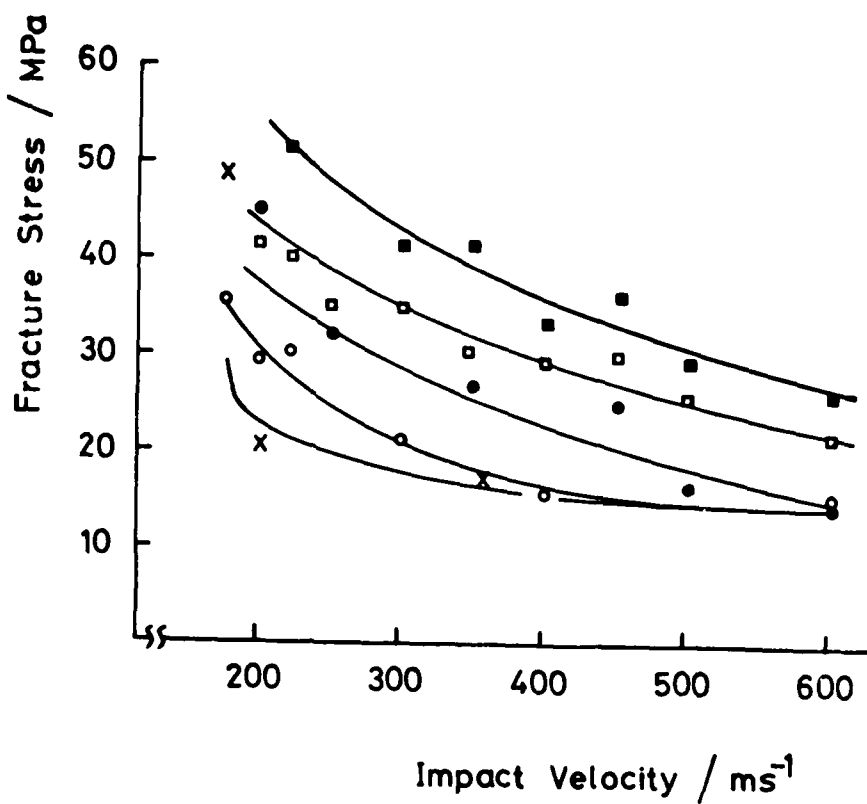


Figure 33. Residual strength curves for multiple impact. Only results for damaged specimens are plotted.

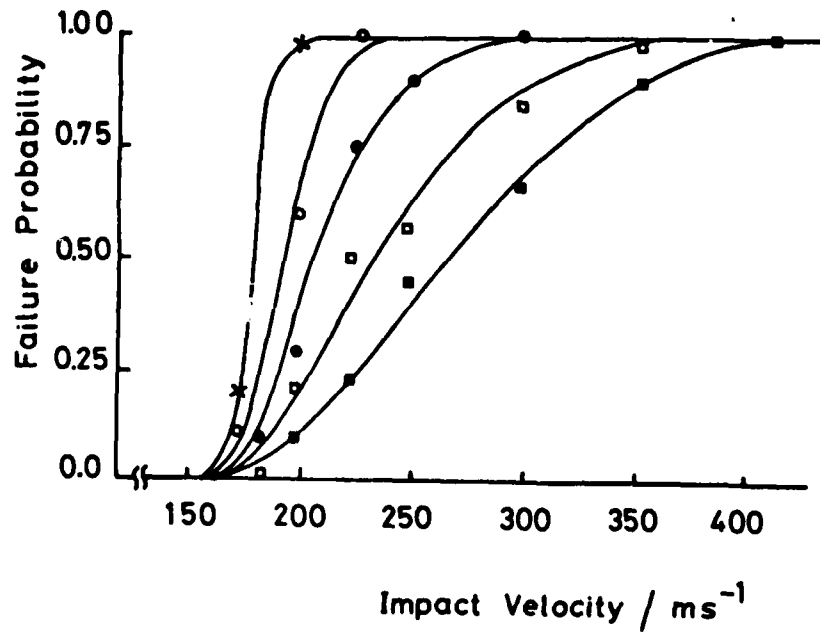


Figure 34. Failure probability for multiple impact by 0.8 mm jet.

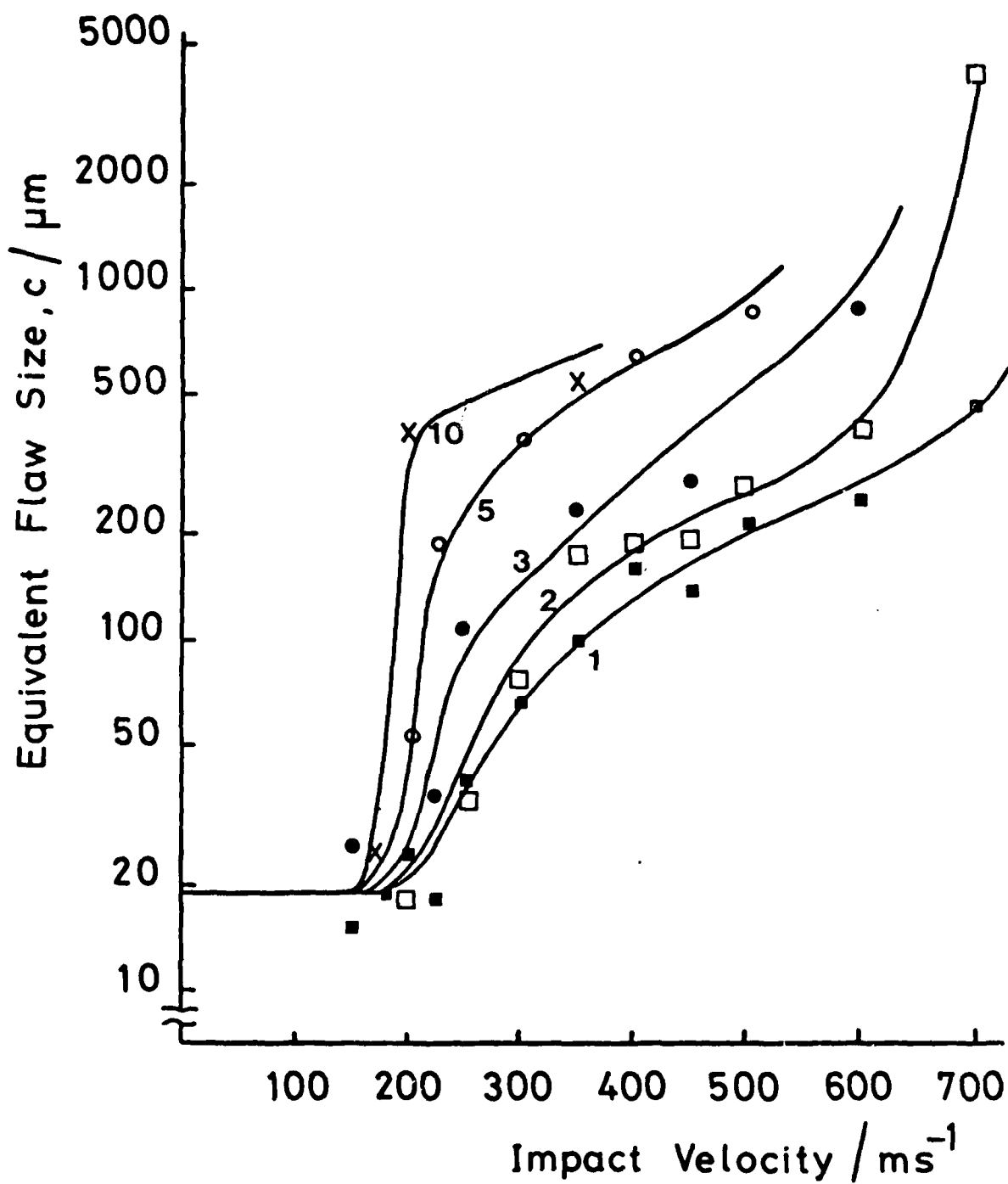


Figure 35. Results of Figure 34 replotted in terms of equivalent flaw size.

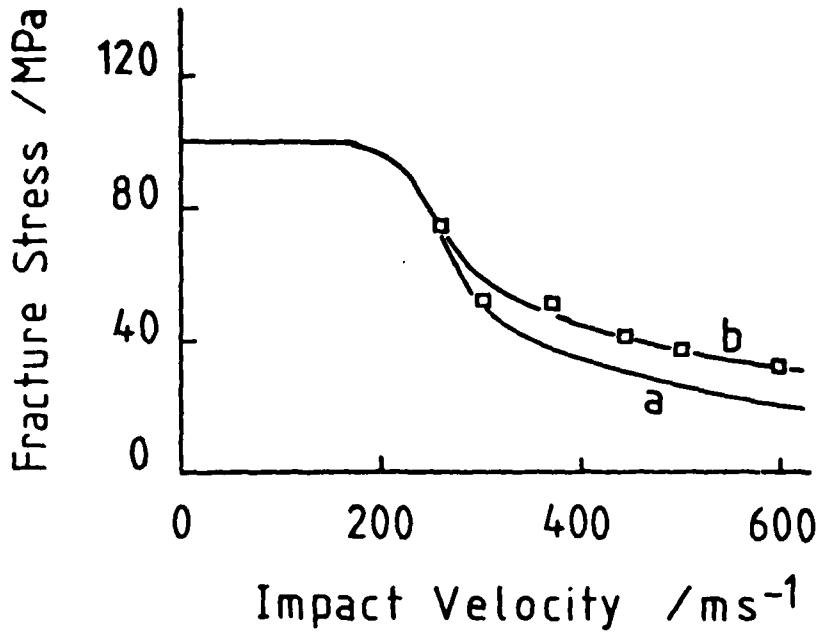


Figure 36. Residual strength curves for 3 mm thick soda-lime-silica glass.  
 (a) specimen supported near its edge.  
 (b) specimen acoustically matched to 25 mm thick glass block.

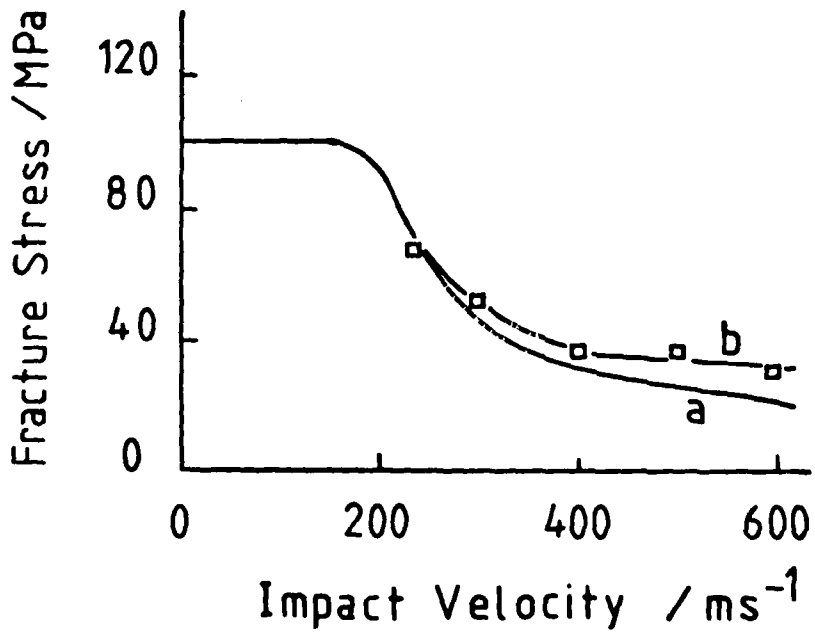


Figure 37. As Figure 36 but now for double impacts per specimen.

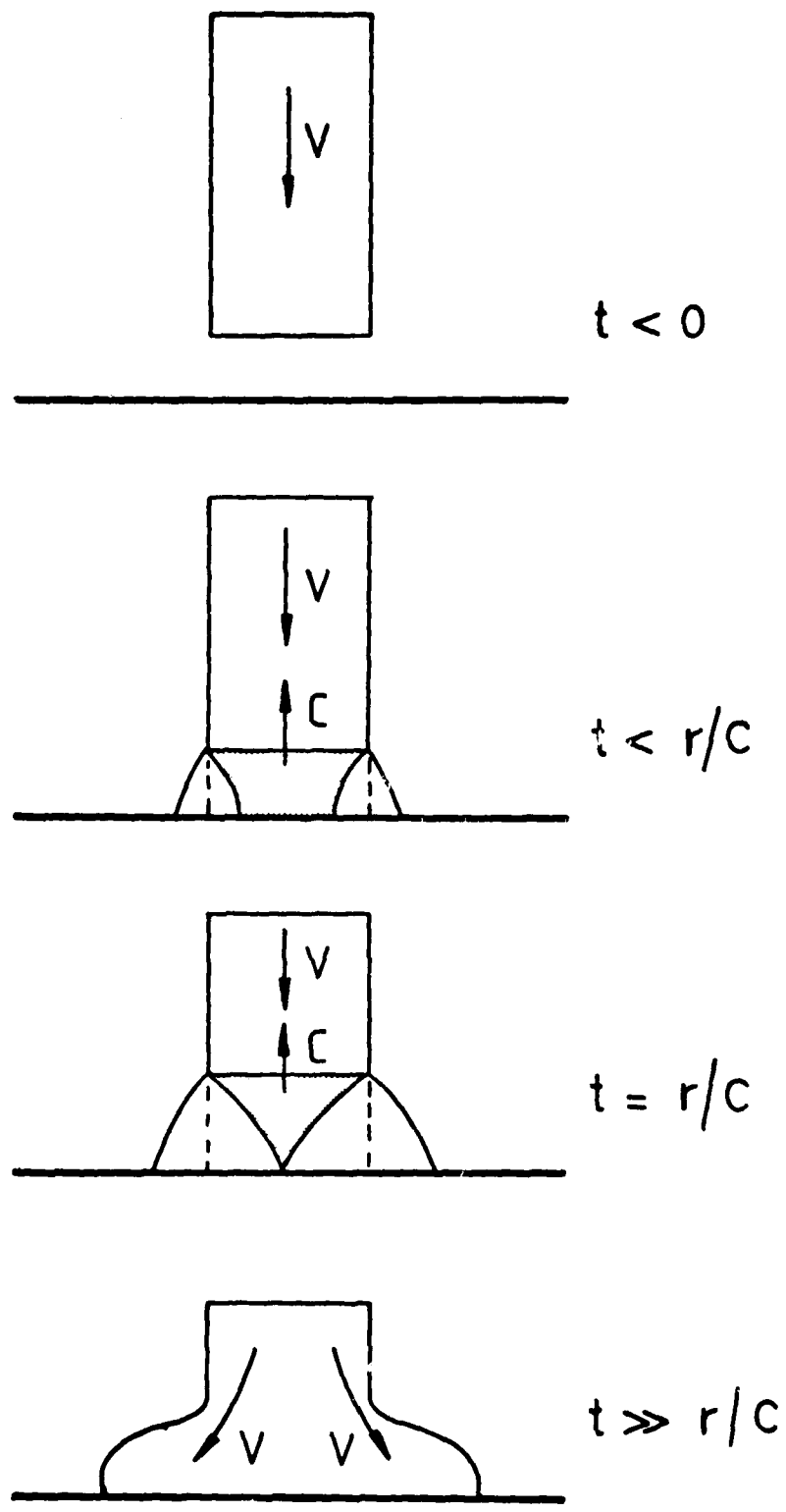


Figure 38. Schematic diagram of the impact process for a flat ended cylindrical jet.

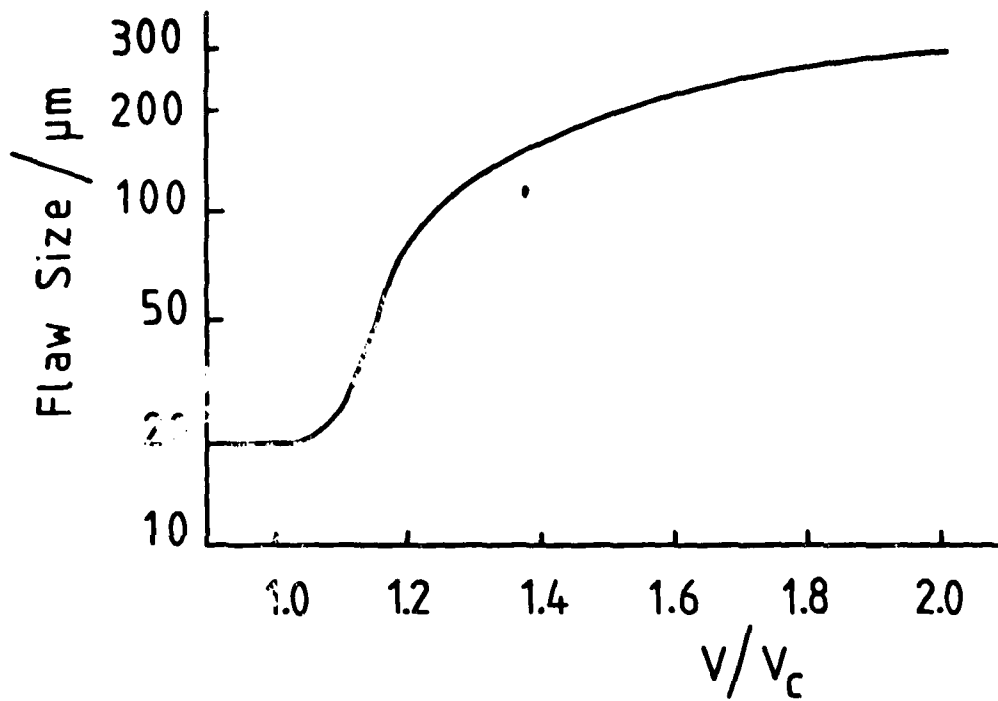


Figure 39. Predicted crack growth for a single 0.8 mm jet impact on soda-lime-silica glass. Initial flaw size 20  $\mu\text{m}$ .

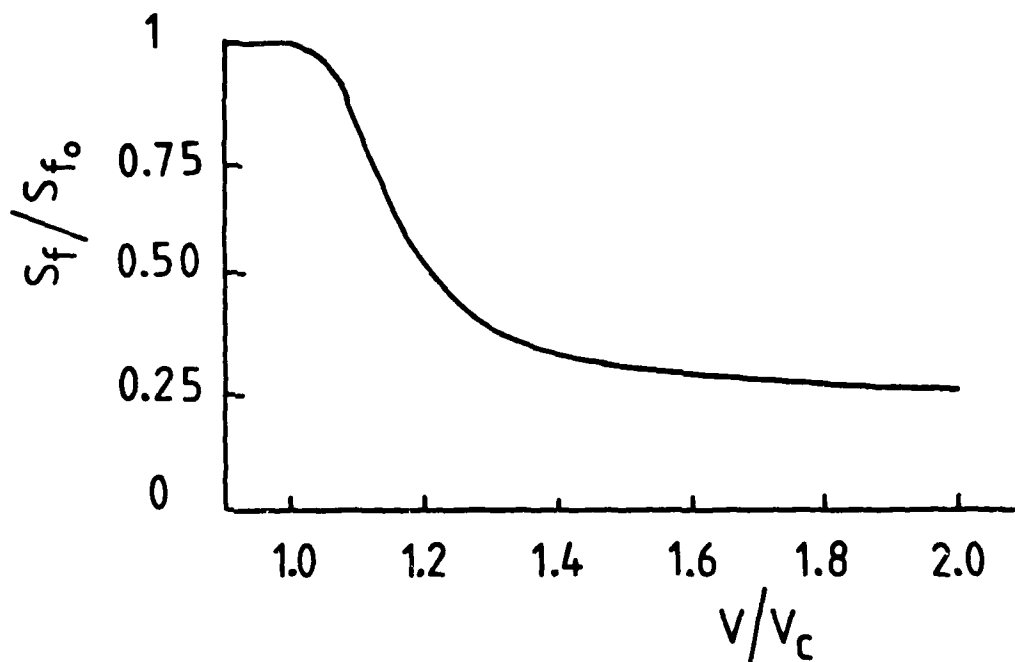


Figure 40. Predicted normalised residual strength curve for 0.8 mm jet impact.

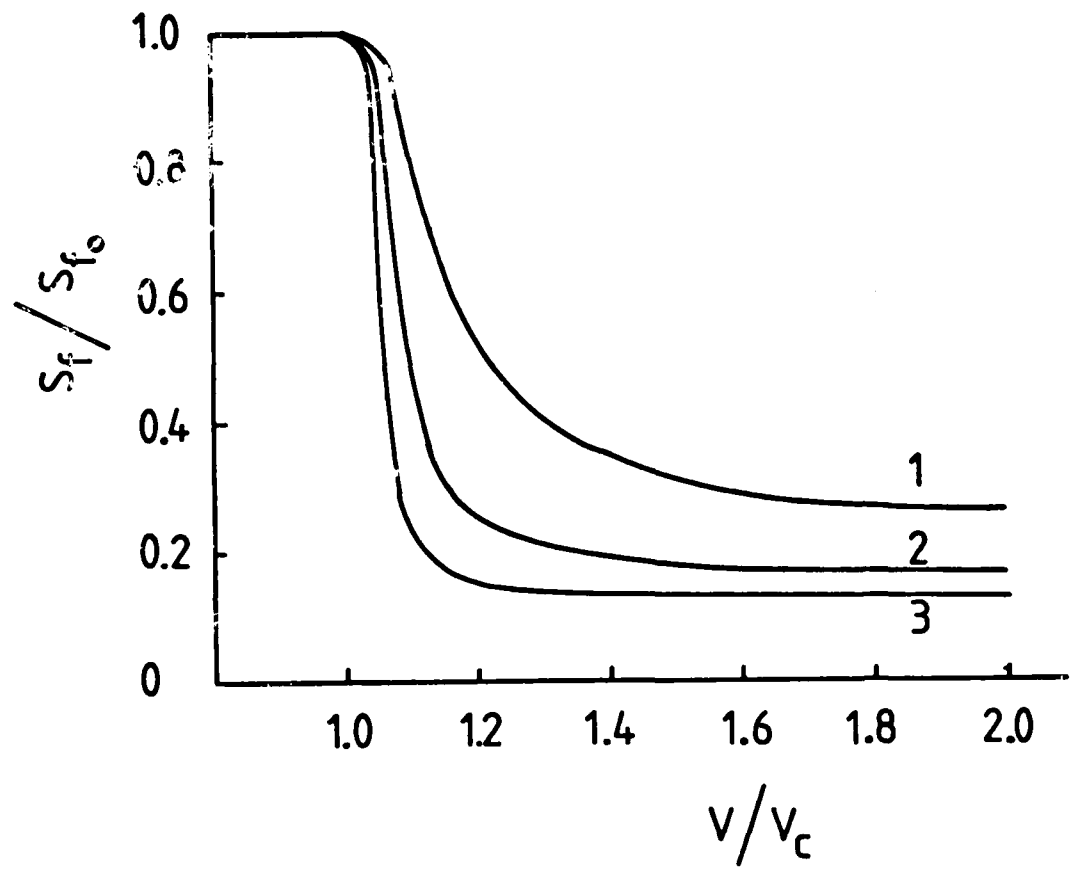


Figure 41. Predicted normalised residual strength curves for 1, 2 and 3 jet impacts per specimen.